An inverse model for calculation of global volume transport from wind and hydrographic data

Peter C. Chu *, Chenwu Fan

Naval Ocean Analysis and Prediction Laboratory, Department of Oceanography, Naval Postgraduate School, Monterey, CA 93943, USA

Abstract

The **P**-vector inverse method has been successfully used to invert the absolute velocity from hydrographic data for the extra-equatorial hemispheres, but not for the equatorial region since it is based on the geostrophic balance. A smooth interpolation scheme across the equator is developed in this study to bring together the two already known solutions (**P**-vectors) for the extra-equatorial hemispheres. This model contains four major components: (a) the **P**-vector inverse model to obtain the solutions for the two extra-equatorial hemispheres, (b) the objective method to determine the Ψ-values at individual islands, (c) the Poisson equation-solver to obtain the Π-values over the equatorial region from the volume transport vorticity equation, and (d) the Poisson equation-solver to obtain the Ψ and depth-integrated velocity field (U, V) over the globe from the Poisson Ψ-equation. The Poisson equation-solver is similar to the box model developed by Wunsch. Thus, this method combines the strength from both box and **P**-vector models. The calculated depth-integrated velocity and Ψ-field agree well with earlier studies.
Published by Elsevier B.V.

1. Introduction

Winds, density, and friction determine volume transport in oceans. The wind-driven volume transport has been estimated using the Sverdrup (1947) relation for the interior ocean, and using the Stommel (1948) and Munk (1950) linear frictional ocean model for the intensive western boundary currents. Leetmaa and Bunker (1978), Meyers (1980), and Godfrey and Golding (1981) calculated similarly for the North Atlantic, tropical Pacific, and Indian Oceans. Baker (1982) examined the

Sverdrup relation in Antarctic regions. Godfrey (1989) used the Sverdrup model with climatological annual winds (Hellerman and Rosenstein 1983) to calculate the mean depth-integrated streamfunction for the world ocean under two assumptions: (1) the ocean is stagnant below some depth, and (2) all major undersea topographic features such as mid-ocean ridges lie below that depth.

The density-driven volume transport has been calculated by several authors. The density field directly determines the geostrophic velocity relative to the bottom flow. The bottom velocity (u_{-H}, v_{-H}) is usually calculated using the β-spiral (Stommel and Schott, 1977), Box (Wunsch, 1978), and **P**-vector (Chu, 1995; Chu et al., 1998a,b; Chu, 2000; Chu et al., 2001a,b; Chu, 2006) models.

---

* Corresponding author.
  E-mail address: pcchu@nps.edu (P.C. Chu).

	Form Approved OMB No. 0704-0188

Report Documentation Page

1. REPORT DATE **SEP 2004**	2. REPORT TYPE	3. DATES COVERED **00-00-2004 to 00-00-2004**

4. TITLE AND SUBTITLE **An inverse model for calculation of global volume transport from wind and hydrographic data**		5a. CONTRACT NUMBER
		5b. GRANT NUMBER
		5c. PROGRAM ELEMENT NUMBER
6. AUTHOR(S)		5d. PROJECT NUMBER
		5e. TASK NUMBER
		5f. WORK UNIT NUMBER
7. PERFORMING ORGANIZATION NAME(S) AND ADDRESS(ES) **Naval Postgraduate School,Department of Oceanography,Monterey,CA,93943**		8. PERFORMING ORGANIZATION REPORT NUMBER
9. SPONSORING/MONITORING AGENCY NAME(S) AND ADDRESS(ES)		10. SPONSOR/MONITOR'S ACRONYM(S)
		11. SPONSOR/MONITOR'S REPORT NUMBER(S)

12. DISTRIBUTION/AVAILABILITY STATEMENT
Approved for public release; distribution unlimited

13. SUPPLEMENTARY NOTES

14. ABSTRACT
The P-vector inverse method has been successfully used to invert the absolute velocity from hydrographic data for the extraequatorial hemispheres, but not for the equatorial region since it is based on the geostrophic balance. A smooth interpolation scheme across the equator is developed in this study to bring together the two already known solutions (P-vectors) for the extraequatorial hemispheres. This model contains four major components: (a) the P-vector inverse model to obtain the solutions for the two extra-equatorial hemispheres, (b) the objective method to determine the ψ-values at individual islands, (c) the Poisson equation-solver to obtain the Π-values over the equatorial region from the volume transport vorticity equation, and (d) the Poisson equation-solver to obtain the ψ and depth-integrated velocity field (U, V) over the globe from the Poisson ψ-equation. The Poisson equation-solver is similar to the box model developed by Wunsch. Thus, this method combines the strength from both box and P-vector models. The calculated depth-integrated velocity and ψ-field agree well with earlier studies.

15. SUBJECT TERMS

16. SECURITY CLASSIFICATION OF:			17. LIMITATION OF ABSTRACT	18. NUMBER OF PAGES	19a. NAME OF RESPONSIBLE PERSON
a. REPORT **unclassified**	b. ABSTRACT **unclassified**	c. THIS PAGE **unclassified**	**Same as Report (SAR)**	**24**	

Since the geostrophic balance is used, these models provide the solutions for the extra-equatorial hemispheres, but not for the equatorial region. An improved inverse method is developed in this study to bring together the two known solutions for the extra-equatorial hemispheres across the equator and to establish a global velocity dataset. The rest of the paper is outlined as follows. Section 2 describes the basic theory of the model. Sections 3–5 describe depth-integrated velocity, volume transport streamfunction, and volume transport vorticity. Section 6 depicts the Ψ-Poisson equation and its solver. Section 7 depicts the model sensitivity. Section 8 provides the global circulation characteristics. Section 9 presents the conclusions.

2. Dynamics

2.1. Basic equations

Let (x, y, z) be the coordinates with x-axis in the zonal direction (eastward positive), y-axis in the latitudinal direction (northward positive), and z-axis in the vertical (upward positive). The unit vectors along the three axes are represented by $(\mathbf{i}, \mathbf{j}, \mathbf{k})$. For the extra-equatorial region, the linear steady state system with the Boussinesq approximation is given by

$$-f(v-v_g) = A_z \frac{\partial^2 u}{\partial z^2} + A_h \nabla^2 u, \tag{1}$$

$$f(u-u_g) = A_z \frac{\partial^2 v}{\partial z^2} + A_h \nabla^2 v, \tag{2}$$

$$\frac{\partial p}{\partial z} = -\rho g, \tag{3}$$

$$\frac{\partial u}{\partial x} + \frac{\partial v}{\partial y} + \frac{\partial w}{\partial z} = 0, \tag{4}$$

where ρ is the *in-situ* density; $f=2\Omega\sin\varphi$, is the Coriolis parameter, Ω the Earth rotation rate, and φ the latitude. $\mathbf{V}=(u, v)$, is the horizontal velocity; w is the vertical velocity; $\nabla = \mathbf{i}\partial/\partial x + \mathbf{j}\partial/\partial y$, is the horizontal gradient operator; $\mathbf{V}_g=(u_g, v_g)$, is the geostrophic velocity representing the horizontal pressure (p) gradients

$$u_g = -\frac{1}{f}\frac{1}{\rho_0}\frac{\partial p}{\partial y}, \quad \mathbf{V}_g = \frac{1}{f}\frac{1}{\rho_0}\frac{\partial p}{\partial x}, \tag{5}$$

where ρ_0 is the characteristic value (1025 kg/m^3) of the sea water density. The two coefficients (A_z, A_h) are the vertical and horizontal eddy diffusivities.

The horizontal diffusivity A_h can be estimated by Smargrinsky parameterization,

$$A_h = \frac{D}{2}\Delta x \Delta y |\nabla \mathbf{V} + (\nabla \mathbf{V})^T|, \tag{6}$$

where

$$|\nabla \mathbf{V} + (\nabla \mathbf{V})^T| \equiv \left[\left(\frac{\partial u}{\partial x}\right)^2 + \frac{1}{2}\left(\frac{\partial v}{\partial x} + \frac{\partial u}{\partial y}\right)^2 + \left(\frac{\partial v}{\partial y}\right)^2\right]^{1/2}.$$

Here, the nondimensional parameter D varies from 0.1 to 0.2 (Mellor, 2003); we set $D=0.15$. The horizontal grid in this study is $1° \times 1°$, i.e., $(\Delta x, \Delta y) \sim 100$ km. Let the spatial variability of the velocity be scaled by 0.1 m s^{-1}, we have

$$|\nabla \mathbf{V} + (\nabla \mathbf{V})^T| \sim 2 \times \frac{0.1 \text{ m s}^{-1}}{10^5 \text{m}} = 2 \times 10^{-6} s^{-1}. \tag{7}$$

Substitution of (7) into (6) leads to

$$A_h = 1.5 \times 10^3 \text{m}^2\text{s}^{-1}. \tag{8}$$

2.2. Ekman number

The Ekman number can identify the relative importance of the horizontal gradient of the Reynolds stress versus the Coriolis force,

$$E = \frac{O(|A_h \nabla^2 \mathbf{V}|)}{O(|f\mathbf{V}|)} = \frac{A_h}{|f|L^2}, \tag{9}$$

where L is the characteristic horizontal length scale. In this study, the motion with L larger than 200 km is considered. For extra-equatorial regions (north of 8°N and south of 8°S),

$$|f| > 0.2 \times 10^{-4} s^{-1},$$

and the Ekman number is estimated by

$$E < \frac{1.5 \times 10^3 \text{m}^2\text{s}^{-1}}{(0.2 \times 10^{-4} s^{-1}) \times (2 \times 10^5 \text{m})^2} = 1.875 \times 10^{-3},$$

which shows that the horizontal gradient of the Reynolds stress can be neglected against the Coriolis force, i.e.,

$$A_h = 0, \tag{10a}$$

for extra-equatorial regions.

For the equatorial regions especially near the equator, $|f|$ is very small. The Ekman number is not a small
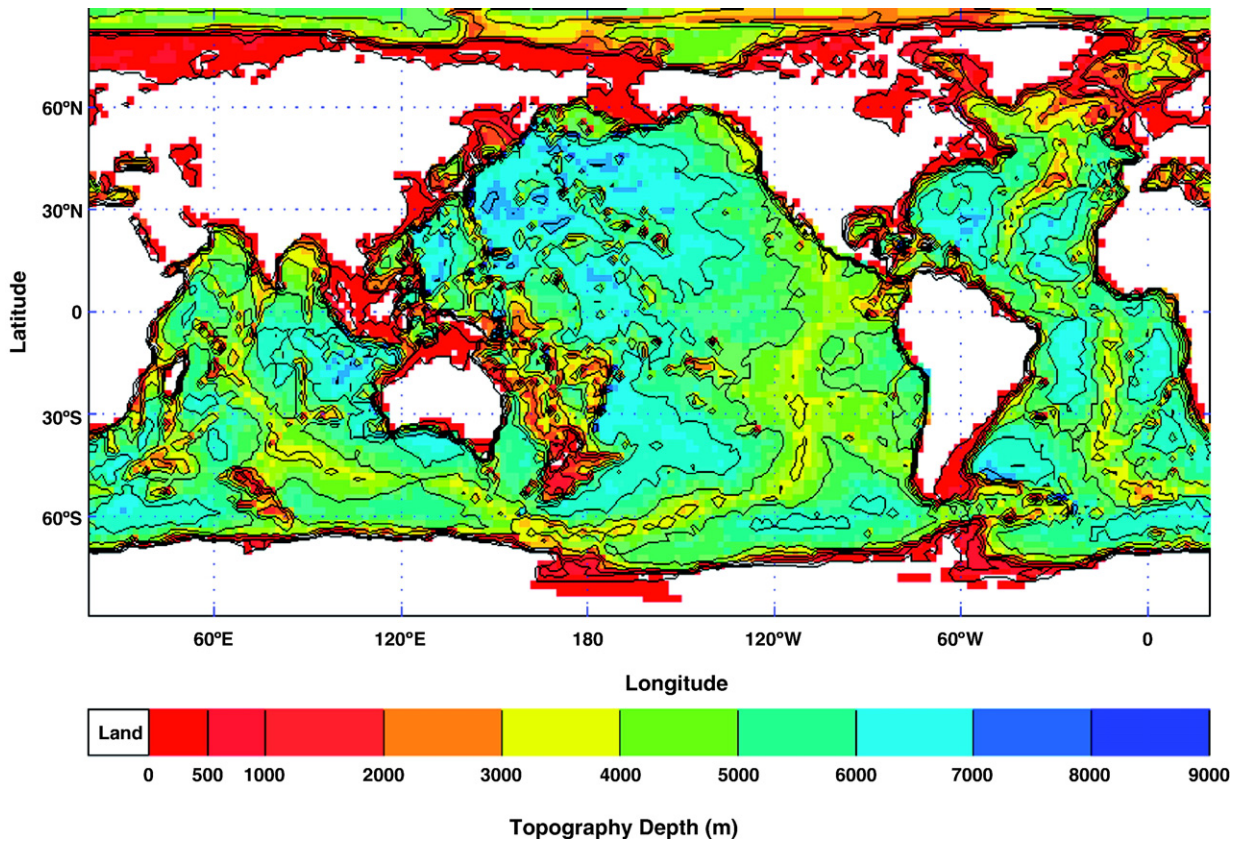
Fig. 1. Bathymetry of world oceans.

parameter. The horizontal viscous force, $(A_h \nabla^2 u, A_h \nabla^2 v)$, cannot be neglected against the Coriolis force in the equatorial region, that is,

$$A_h \neq 0, \tag{10b}$$

for the equatorial regions.

3. Depth-integrated velocity

Let (U, V) and (U_g, V_g) be the depth-integrated horizontal velocity

$$(U, V) = \int_{-H}^{0} (u, v) dz, \tag{11}$$

and geostrophic velocity,

$$(U_g, V_g) = \int_{-H}^{0} (u_g, v_g) dz, \tag{12}$$

where $z = -H(x, y)$ represents the ocean bottom, and $z = 0$ refers to the ocean surface. Depth-integration of (1) and (2) from the ocean bottom to the ocean surface leads to
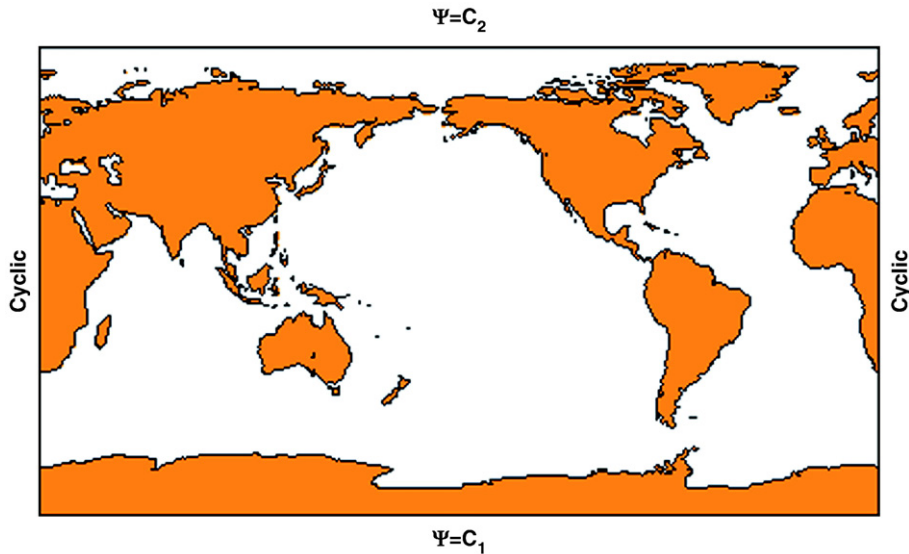
$$-f(V - V_g) = A_z \frac{\partial u}{\partial z}\Big|_{z=\eta} - A_z \frac{\partial u}{\partial z}\Big|_{z=-H} + A_h \nabla^2 U \\ - 2A_h \nabla u_{-H} \bullet \cdot \nabla H - A_h u_{-H} \nabla^2 H, \tag{13}$$

$$f(U - U_g) = A_z \frac{\partial v}{\partial z}\Big|_{z=\eta} - A_z \frac{\partial v}{\partial z}\Big|_{z=-H} + A_h \nabla^2 V \\ - 2A_h \nabla v_{-H} \bullet \cdot \nabla H - A_h v_{-H} \nabla^2 H, \tag{14}$$

where (u_{-H}, v_{-H}) are velocity components at the ocean bottom.

The turbulent momentum flux at the ocean surface is calculated by

$$A_z \left(\frac{\partial u}{\partial z}, \frac{\partial v}{\partial z} \right)\Big|_{z=\eta} = \frac{(\tau_x, \tau_y)}{\rho_0}, \tag{15}$$

$$\Psi = C_2$$

Fig. 2. Boundary conditions of Ψ for the global ocean.

where (τ_x, τ_y) are the surface wind stress components. The turbulent momentum flux at the ocean bottom is parameterized by

$$A_z \left(\frac{\partial u}{\partial z}, \frac{\partial v}{\partial z} \right) \Big|_{z=-H}$$
$$= C_D \sqrt{u_{-H}^2 + v_{-H}^2} (u_{-H}, v_{-H}), \qquad (16)$$

where $C_D = 0.0025$ is the drag coefficient.

The thermal wind relation can be obtained from vertical integration of the hydrostatic balance Eq. (3) from the bottom $(-H)$ to any depth (z) and then the use of the geostrophic Eq. (5)

$$u_g = u_{-H} + \frac{g}{f \rho_0} \int_{-H}^{z} \frac{\partial \rho}{\partial y} dz', \qquad (17)$$

$$v_g = v_{-H} - \frac{g}{f \rho_0} \int_{-H}^{z} \frac{\partial \rho}{\partial x} dz'. \qquad (18)$$

Substitution of (17) and (18) into the second equation of (12) leads to

$$(U_g, V_g) = (U_{den} + Hu_{-H}, V_{den} + Hv_{-H}), \qquad (19)$$

where

$$(U_{den}, V_{den})$$
$$= \frac{g}{f \rho_0} \left(\int_{-H}^{0} \int_{-H}^{z} \frac{\partial \rho}{\partial y} dz' dz, \quad - \int_{-H}^{0} \int_{-H}^{z} \frac{\partial \rho}{\partial x} dz' dz \right), \qquad (20)$$

is the density-driven transport. Re-arranging (13) and (14), we have

$$A_h \nabla^2 U + fV = fV_{den} + fV_b - \frac{\tau_x}{\rho_0} + A_h Q_1, \qquad (21)$$

$$-A_h \nabla^2 V + fU = fU_{den} + fU_b + \frac{\tau_y}{\rho_0} - A_h Q_2, \qquad (22)$$

where

$$Q_1 \equiv (2 \nabla u_{-H} \bullet \cdot \nabla H + u_{-H} \nabla^2 H),$$

$$Q_2 \equiv (2 \nabla v_{-H} \bullet \cdot \nabla H + v_{-H} \nabla^2 H),$$

and

$$U_b = \left(H - \frac{C_D}{f} \sqrt{u_{-H}^2 + v_{-H}^2} \right) u_{-H}, \qquad (23)$$

$$V_b = \left(H + \frac{C_D}{f} \sqrt{u_{-H}^2 + v_{-H}^2} \right) v_{-H},$$

are the transport due to the bottom currents, or simply called the bottom transport. With the known bottom velocity vector (u_{-H}, v_{-H}), the depth-integrated velocity (U, V) can be determined from the wind, density, and topographic data.
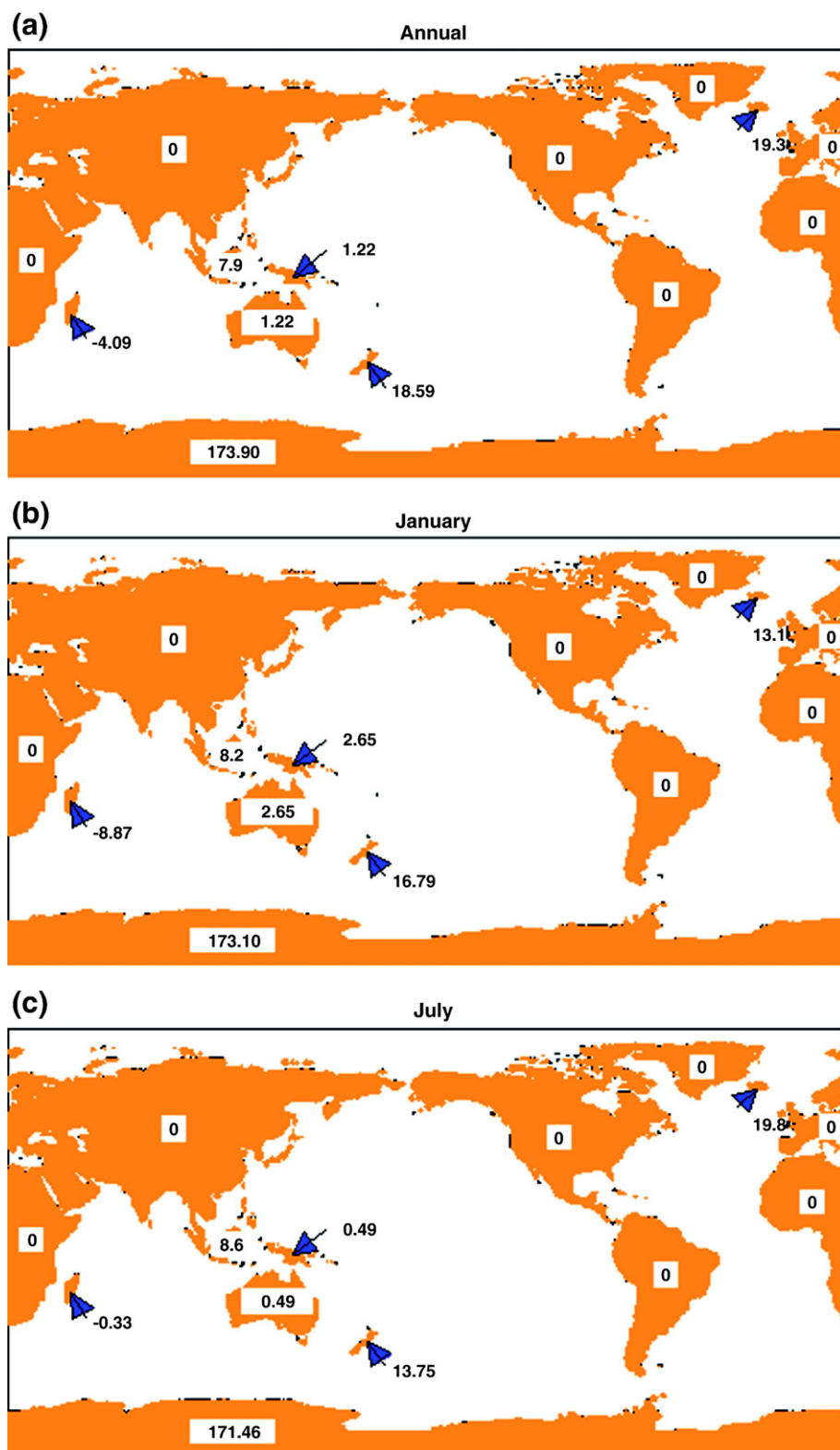
Fig. 3. Computed Ψ-values for each continent/island: (a) annual mean, (b) January, and (c) July.

For the extra-equatorial regions, the horizontal diffusion can be neglected [see (8)]. Eqs. (22) and (21) become

$$U^* = U_{den} + U_b + \frac{\tau_y}{f\rho_0}, \tag{24}$$

$$V^* = V_{den} + V_b - \frac{\tau_x}{f\rho_0}. \tag{25}$$

With the known (u_{-H}, v_{-H}), the depth-integrated flow (U^*, V^*) may be directly calculated using (24) and (25). However, the computed (U^*, V^*) field using (24) and (25) is quite noisy and cannot not be the final product. Thus, the subscript '*' is used to represent the interim depth-integrated velocity calculated using (24) and (25).

4. Volume transport streamfunction

Integration of the continuity equation with respect to z from the bottom to the surface yields,

$$\frac{\partial U}{\partial x} + u_{-H}\frac{\partial H}{\partial x} + \frac{\partial V}{\partial y} + v_{-H}\frac{\partial H}{\partial y} - w_{-H} = 0. \tag{26}$$

With the assumption that the water flows following the bottom topography,

$$w_{-H} = u_{-H}\frac{\partial H}{\partial x} + v_{-H}\frac{\partial H}{\partial y},$$

Eq. (26) becomes

$$\frac{\partial U}{\partial x} + \frac{\partial V}{\partial y} = 0,$$

which leads to the definition of the volume transport streamfunction Ψ,

$$U = -\frac{\partial \Psi}{\partial y}, \quad V = \frac{\partial \Psi}{\partial x}. \tag{27}$$

Subtraction of the differentiation of (22) with respect to y from the differentiation of (21) with respect to x gives

$$\nabla^2 \Psi = \Pi, \tag{28}$$

where

$$\Pi \equiv \frac{1}{f}\left[\frac{\partial(fV_{den})}{\partial x} - \frac{\partial(fU_{den})}{\partial y}\right] + \frac{1}{f}\left[\frac{\partial(fV_b)}{\partial x} - \frac{\partial(fU_b)}{\partial y}\right]. $$
$$-\frac{1}{f}\left[\frac{\partial}{\partial x}\left(\frac{\tau_x}{\rho_0}\right) + \frac{\partial}{\partial x}\left(\frac{\tau_y}{\rho_0}\right)\right]$$
$$+\frac{A_h}{f}\left(\frac{\partial Q_1}{\partial x} + \frac{\partial Q_2}{\partial y}\right), \tag{29}$$

is the volume transport vorticity. Eq. (28) is called the Poisson Ψ-equation.

5. Volume transport vorticity

5.1. Volume transport vorticity equation

Summation of the differentiation of (21) with respect to y and the differentiation of (22) with respect to x gives the volume transport vorticity equation,

$$\nabla^2 \Pi = \frac{\beta}{A_h}(V - V_{den} - V_b) - \frac{1}{A_h\rho_0}\left(\frac{\partial \tau_y}{\partial x} - \frac{\partial \tau_x}{\partial y}\right)$$
$$+\left(\frac{\partial Q_2}{\partial x} - \frac{\partial Q_1}{\partial y}\right), \tag{30}$$

where $\beta = df/dy$, and (28) is used.

5.2. Extra-equatorial region

For the extra-equatorial region, the horizontal diffusion can be neglected [see (8)]. Substitution of A_h into 0 leads to

$$\Pi \equiv \frac{1}{f}\left[\frac{\partial(fV_{den})}{\partial x} - \frac{\partial(fU_{den})}{\partial y}\right]$$
$$+\frac{1}{f}\left[\frac{\partial(fV_b)}{\partial x} - \frac{\partial(fU_b)}{\partial y}\right] - \frac{1}{f}\left[\frac{\partial}{\partial x}\left(\frac{\tau_x}{\rho_0}\right) + \frac{\partial}{\partial x}\left(\frac{\tau_y}{\rho_0}\right)\right]. \tag{31}$$

Similarly, (30) becomes

$$\beta(V - V_{den} - V_b) = \frac{1}{\rho_0}\left(\frac{\partial \tau_y}{\partial x} - \frac{\partial \tau_x}{\partial y}\right), \tag{32}$$

which is the Sverdrup relation.

In (31), (U_{den}, V_{den}) depend on ρ only; (τ_x, τ_y) are wind stress components; and (U_b, V_b) are determined by the bottom current velocity (u_{-H}, v_{-H}). The **P**-vector inverse method (Chu, 1995; Chu et al., 1998a,b; Chu, 2000) is used to determine (u_{-H}, v_{-H}) from hydrographic data (see Appendix A). In this study, the climatological hydrographic data (Levitus et al., 1994) are used to compute (U_{den}, V_{den}) [see (20)]. The climatological surface wind stress (τ_x, τ_y) data are obtained from the Comprehensive Ocean-Atmosphere Data Set (COADS, da Silva et al., 1994). The bottom topography is obtained from the Navy's Digital Bathymetry Data Base 5-min (DBDB5) (Fig. 1). The volume transport vorticity Π is quite noisy.
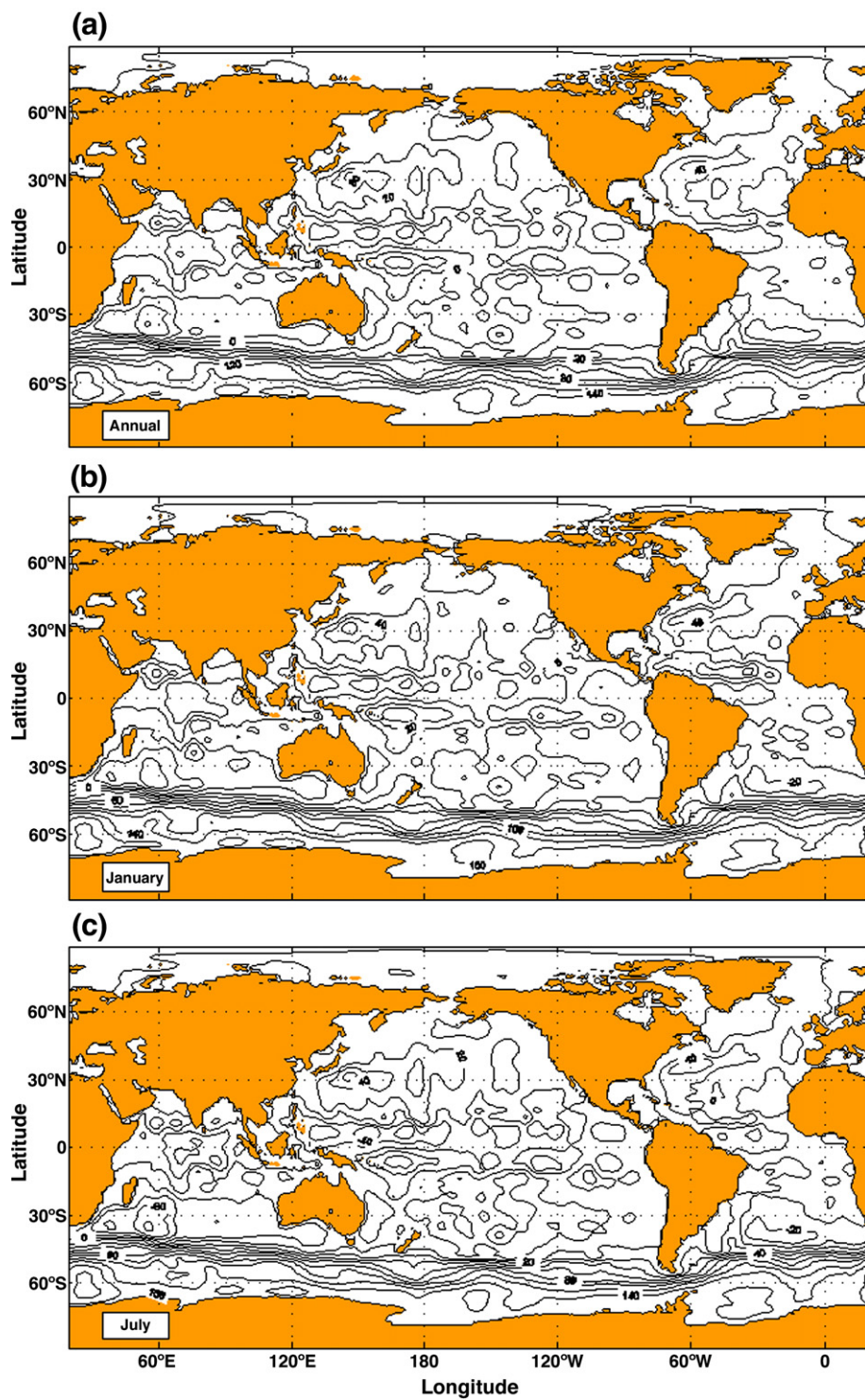
Fig. 4. Global volume transport stream function (Ψ) computed from the inverse model: (a) annual mean, (b) January, and (c) July.

5.3. Equatorial region (between 8°S and 8°N)

Let the volume transport vorticity Π calculated using (31) at 8°N and 8°S as the northern and southern boundary values of the vorticity Eq. (30). Here, the forcing terms [righthand-side of (30)] are calculated with the assumptions that (1) $f=f(8°N)$ north of the equator, and $f=f(8°S)$ south of the equator, and
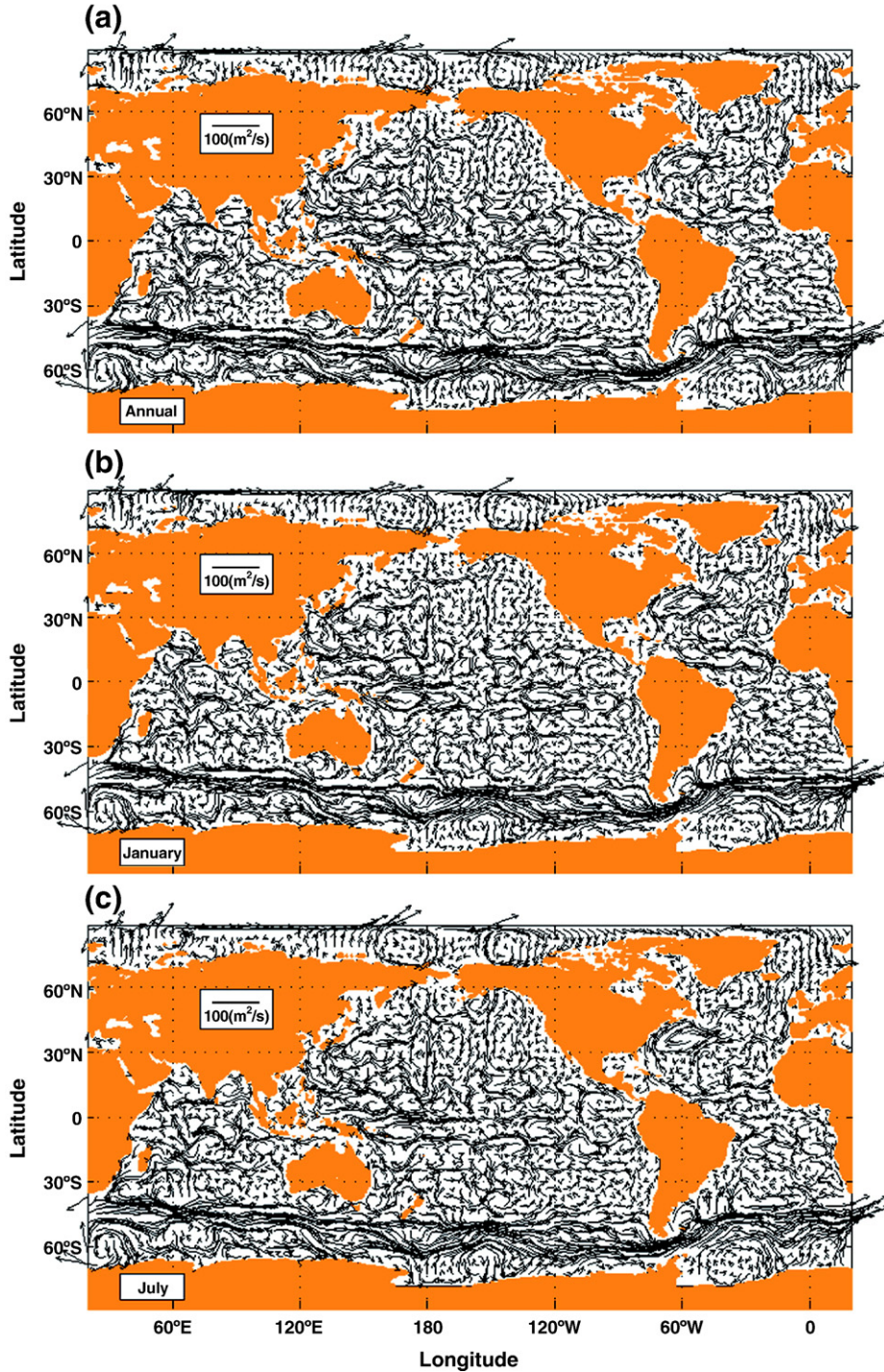

Fig. 5. Global depth-integrated velocity (U, V) vectors computed from the inverse model: (a) annual mean, (b) January, and (c) July.

(2) (U, V) are calculated by (24) and (25). With the given forcing terms and the northern and southern boundary conditions and the cyclic eastern and western boundary conditions, the volume transport vorticity Eq. (30) can be solved in the equatorial region between 8°N and 8°S. The computed Π-field is quite smooth.

6. Poisson Ψ-equation

6.1. Boundary conditions

With the computed global volume transport vorticity (Π), the Poisson Ψ-equation (28) can be solved when the boundary conditions are given. No flow over the Antarctic Continent leads to the southern boundary condition

$$\Psi = C_1, \text{ at the southern boundary } y = y_s. \quad (33)$$

No horizontal convergence of the 2-dimensional flow (U, V) at the North Pole (treated as an island) leads to the northern boundary condition

$$\Psi = C_2, \text{ at the northern boundary } y = y_n, \quad (34)$$

where C_1 and C_2 are the constants to be determined. The cyclic boundary condition is applied to the western and the eastern boundaries (Fig. 2). We integrate $\partial \Psi / \partial y = -U^*$ with respect to y along the western (or eastern) boundary from the southern boundary ($\Psi = 0$) to the northern boundary to obtain

$$\Psi|_{\text{west}}(y) = - \int_{y_s}^{y} U^*(x_{\text{west}}, y') \mathrm{d}y'. \quad (35)$$

The cyclic boundary condition leads to

$$\Psi|_{\text{east}}(y) = \Psi|_{\text{west}}(y). \quad (36)$$

Thus, the northern boundary condition is given by

$$\Psi = - \int_{y_s}^{y_n} U^*(x_{\text{west}}, y) \mathrm{d}y = C_2. \quad (37)$$

6.2. Ψ-Values at islands

Before solving the Poisson Ψ-equation (28) with the boundary conditions (33)–(35) and (37), we need to know the Ψ-values at all islands. These values were subjectively set up in some earlier studies. For example, in calculating the geostrophic transport in the Pacific Ocean, Reid (1997) set up Ψ-value to be 0 for Antarctic, 135 Sv (1 Sv = 10^6 m^{3}s^{-1}) for Australia, and 130 Sv for America. In calculating the geostrophic transport in the South Atlantic Ocean, Reid (1989) set up Ψ-value to be 0 for Antarctic, 132 Sv for Africa, and 130 Sv for America. Such a treatment subjectively prescribes 130 Sv through the Drake Passage and 132 Sv through area between Africa and Antarctica.

An objective method depicted in Appendix-B is used to determine Ψ-values at islands. Fig. 3 shows the distribution of Ψ-value for each continent/island computed from the annual, January, and July mean hydrographic and wind data. Taking the annual mean as an example, we have: 0 for the American Continent, 157.30 Sv for Antarctica, −21.74 Sv for Australia, −27.17 Sv for Madagascar, and −21.74 Sv for New Guinea.

7. Model sensitivity

With the given values at the boundaries and islands, we solve the Poisson Ψ-equation (28) with climatological annual and monthly Π-fields and obtain annual and
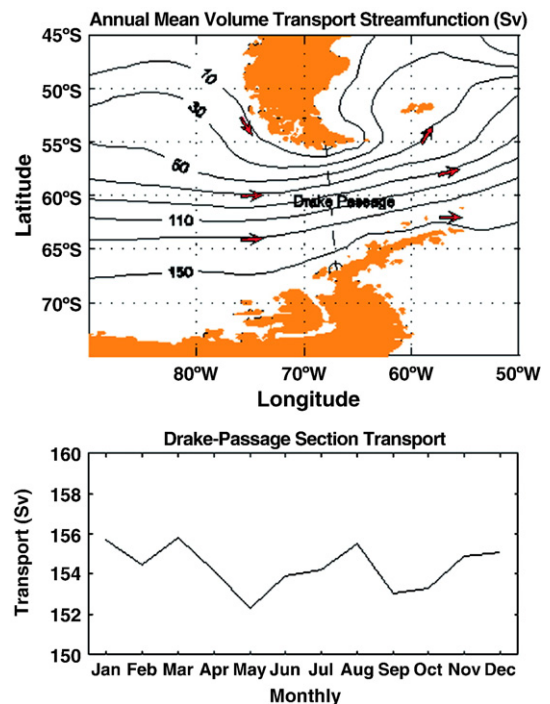

Fig. 6. Monthly volume transport through the Drake Passage with a small seasonal variation.

monthly global Ψ-fields. After that, we use (27) to re-compute the depth-integrated velocity (U, V). Since 1° × 1° hydrographic (Levitus and Boyer, 1994; Levitus et al., 1994) and wind data (da Silva et al., 1994) are used to compute Ψ-fields, small-scale topographic features such as English Channel, Taiwan Strait, Gilbralta Strait, and Bering Strait cannot be resolved in this study. Here, we present the annual and monthly (January and July) mean Ψ-fields obtained using the inverse model. The global Ψ-field (Fig. 4) and depth-integrated velocity vector (U, V) field (Fig. 5) agree reasonably well with earlier studies (e.g., Reid, 1989; Semtner and Chervin, 1992; Reid, 1994, 1997) and shows the capability of the inverse model for determin-ing main characteristics of global circulation such as the strong Antarctic Circumpolar Current, the well-defined subtropical and subpolar gyres, and the equatorial current system. We will discuss these features for each ocean basin in Section 8.

The hydrographic and wind data contain errors (observational errors). The horizontal diffusion coeffi-cient A_h is uncertain. Sensitivity study is conducted on the solutions to uncertain A_h and the observational data before discussing the calculated circulation character-istics. First, the model is integrated with different values of the horizontal diffusivity A_h. There is almost no difference among the Ψ-fields with different values of diffusivity A_h between 1.5×10^3 and 5×10^5 m^2 s^{-1}.
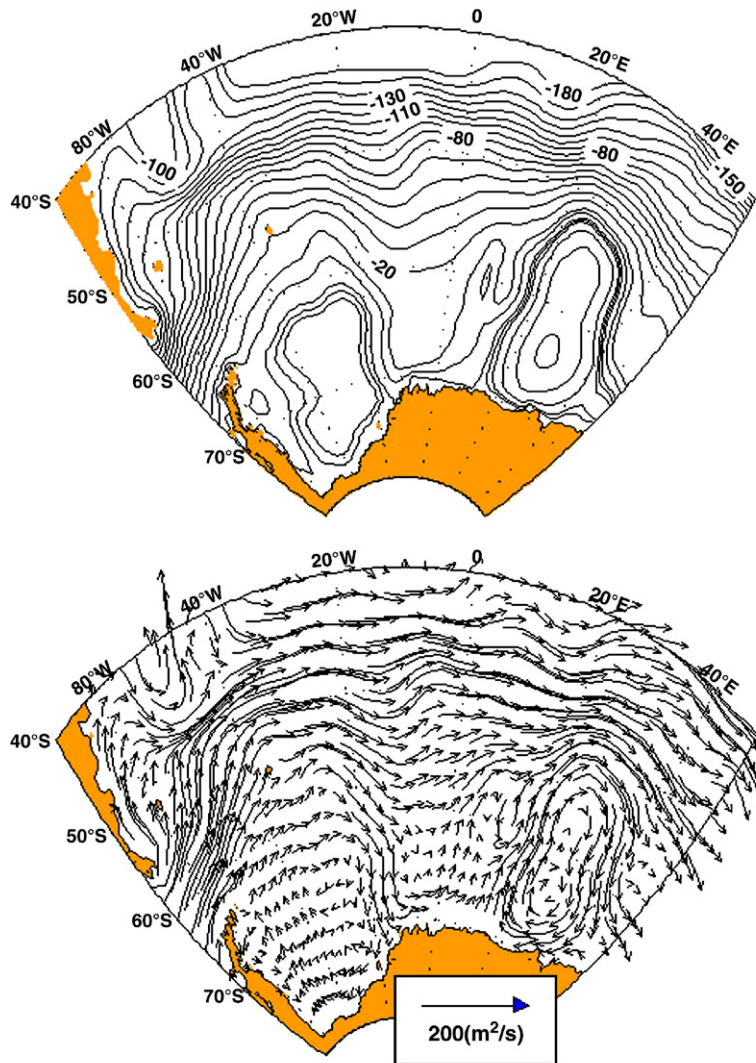

Fig. 7. Inverted January Ψ and (U, V) vector fields in the Weddell Sea.
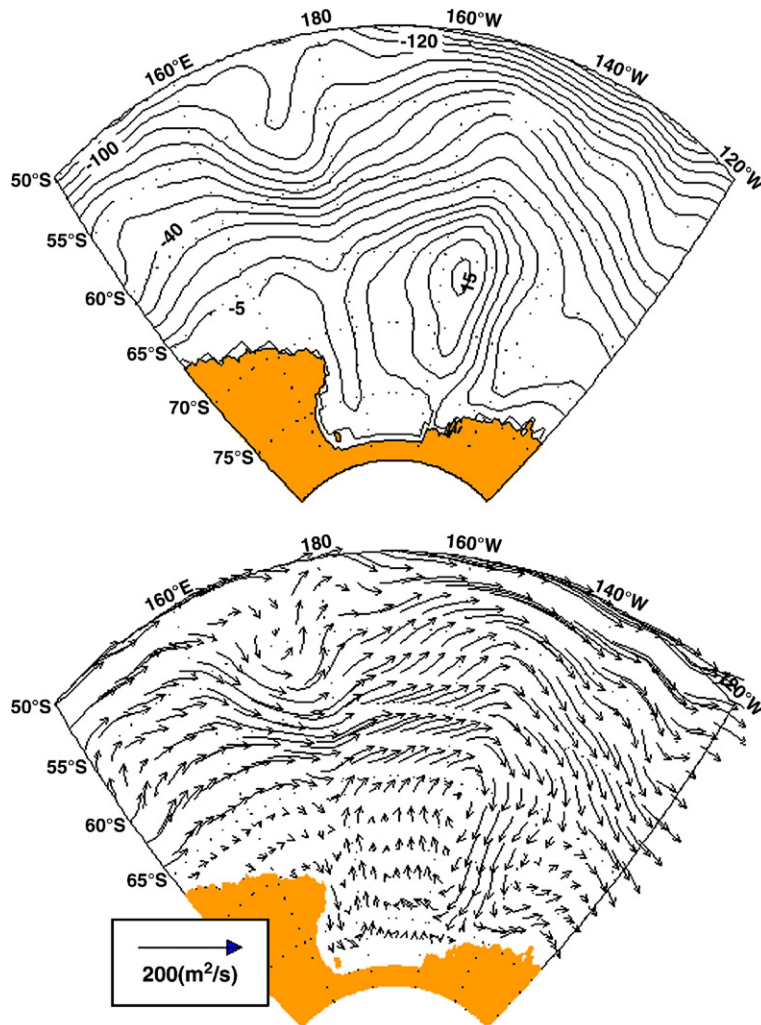
Fig. 8. Inverted January Ψ and (U, V) vector fields in the Ross Sea.

Second, suppose the observational data errors to be represented by a Gaussian-type random variable $(\delta\chi)$ with a zero mean and a standard deviation of σ whose probability distribution function is given by

$$F(\delta\chi) = \frac{1}{\sqrt{2\pi}} \exp\left[-\frac{(\delta\chi)^2}{2\sigma^2}\right]. \tag{38}$$

In this study, a random number generator (FORTRAN function, Ranf) is used to produce two sets of random noises for each grid point independently, with mean value of zero and standard deviation of σ: (a) three-dimensional temperature error field with standard deviation of 0.2 °C and (b) two dimensional surface wind stress error field with standard deviation of

0.05 N m^{-2}. The model stability is confirmed from almost no difference between the Ψ-field with random errors in temperature and/or surface wind stress data and the Ψ-field with no error added. Thus, this inverse model has the capability to filter out noise in the forcing terms because of the major mathematical procedures of the model containing two integrations of the Poisson equation.

8. Global circulation characteristics

The depth-integrated velocity vector field (U, V) is presented to illustrate the capability of this inverse model. However, it is not our intention to review the general circulation features. Interested readers are referred to Schmitz (1996a,b).

8.1. Southern Ocean

8.1.1. Antarctic Circumpolar Currents at the Drake Passage

The computed monthly mean volume transport through the Drake Passage is around 156 Sv with a small seasonal variation (Fig. 6), which compares well with the estimate of 134 Sv by Nowlin and Klink (1986), although observed Antarctic Circumpolar Current transports are subject to uncertainties of tens of Sverdrups depending on the contribution of weak flows at depth.

8.1.2. Weddell cyclonic (clockwise) gyre

In the Weddell Sea, which probably contributes most to bottom water formation, the water flows westward under the influence of the Coriolis force as it sinks, forming a thin layer of extremely cold water above the continental slope. It mixes with the overlying water, which is recirculated with the large cyclonic eddy in the central Weddell Sea. The Weddell Sea is one of the few places in the world ocean where deep and bottom water masses are formed to participate in the global thermohaline circulation. The characteristics of exported water masses are the result of complex interactions among surface forcing, significantly modified by sea ice, ocean dynamics at the continental shelf break and slope (Foldvik et al., 1985; Muench and Gordon, 1995) and sub-ice shelf water mass transformation.

The most striking feature of the inverted January mean Ψ and (U, V) fields in the Weddell Sea (Fig. 7) is the existence of the double-cell structure of the Weddell Gyre as suggested by the hydrographic observations (Mosby, 1934; Deacon, 1979; Bagriantsev et al., 1989) and the numerical simulation of a regional coupled ice-ocean model (Beckmann et al., 1999). Our computation shows one cell filling the western Weddell Basin and the other trapped in a deeper basin northeast of Maud Rise. The west cell and the east cell circulate 4–5 Sv and 30 Sv, respectively. The west cell is weaker than earlier studies (e.g., Beckmann et al., 1999).

8.1.3. Ross cyclonic (clockwise) gyre

The Ross Sea and adjacent Southern Ocean represent important areas of biogenic production and potentially large sources of biogenic material to the water column and sediments. Current meter moorings show that the general circulation in the Ross Sea surface waters is cyclonic, with a slow southward flow in the central and eastern Ross Sea (Pillsbury and Jacobs, 1985). On the basis of moored current meter data, DeMaster et al. (1992) pointed out the following facts: the flow in the southern Ross Sea is typically westward. This circula-

tion is well developed in the surface waters and extends to depth as well. Current speeds at 40 m above the seabed are relatively low, on the order of 0.1 m s^{-1}. The inverted January circulation patterns (Fig. 8) shows that the Ross Sea cyclonic gyre recirculates 15–30 Sv, which agrees well with Reid (1997).

8.2. Pacific Basin

8.2.1. General features

The annual mean northward transport across the equator in the west is 21.7 Sv, between the −21.7 Sv isoline at the western boundary (northeast coast of New Guinea) to the 0 Sv isoline near 170°W (Fig. 4a). This current meanders and generates several eddies such as the Mindanao Eddy (cyclonic) near southern Philippines and the Halmahera Eddy (anticyclonic) near Indonesia. The northward current joins the North Equatorial Current with 30 Sv transport (from 0 to 30 Sv isoline) east of the Philippines (10°–15°N). Of these 51.7 Sv of water, 21.7 Sv are lost to the Indonesian seas directly, or via the South China Sea indirectly. The remaining 30 Sv of water continues northward to Japan and then eastward with the anticyclonic gyre. This subtropical gyre recirculates 20 Sv between 25°–35°N (from 30 to 50 Sv isoline) and makes 50 Sv of the Kuroshio Current east of Japan. Longitudinal dependence of Ψ along the dateline and 150°W (Fig. 9) in the equatorial region show the existence of the westward flowing South Equatorial Current ($\Delta \Psi / \Delta y > 0$) between 3°S and 12°S, eastward flowing Equatorial Counter Current ($\Delta \Psi / \Delta y < 0$) between 3°S and 2°N, and westward flowing North Equatorial Current ($\Delta \Psi / \Delta y > 0$) between 2°N and 12°N.
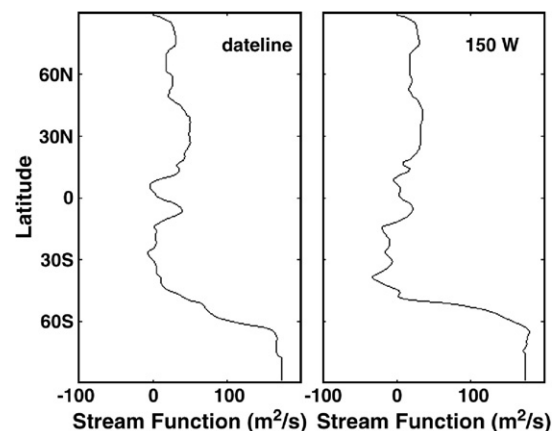

Fig. 9. Annual mean volume transport streamfunction at dateline and 150°W.

There are several low-latitude cyclonic gyres, with axes along 8°N and 8°S. Among them, an evident cyclonic gyre occurs in the north equatorial region between 180°–120°E, and three smaller cyclonic eddies (also called broken gyres) appear in the south equatorial region, east of 170°E. The north equatorial gyre appeared clearly on the study by Munk (1950) of the wind-driven circulation of the North Pacific, and was identified by Reid (1997) using hydrographic data. The south equatorial gyre identified in this study (broken gyre) is different from Reid's (1997) and Tsuchiya's

(1968) description of a complete gyre structure. The south subtropical anticyclonic gyre occurs east of 180°E between 12°S and 45°S and recirculates 30 Sv of water.

8.2.2. Pacific–Indian Ocean throughflow region

The Indonesian throughflow is the only inter-basin exchange of water at low-latitudes from the Pacific to the Indian Ocean. The calculated monthly mean Ψ and (U, V) fields in the vicinity of Indonesia (Fig. 10) shows the volume transport and the depth-integrated circulation pattern have weak seasonal variations and are quite
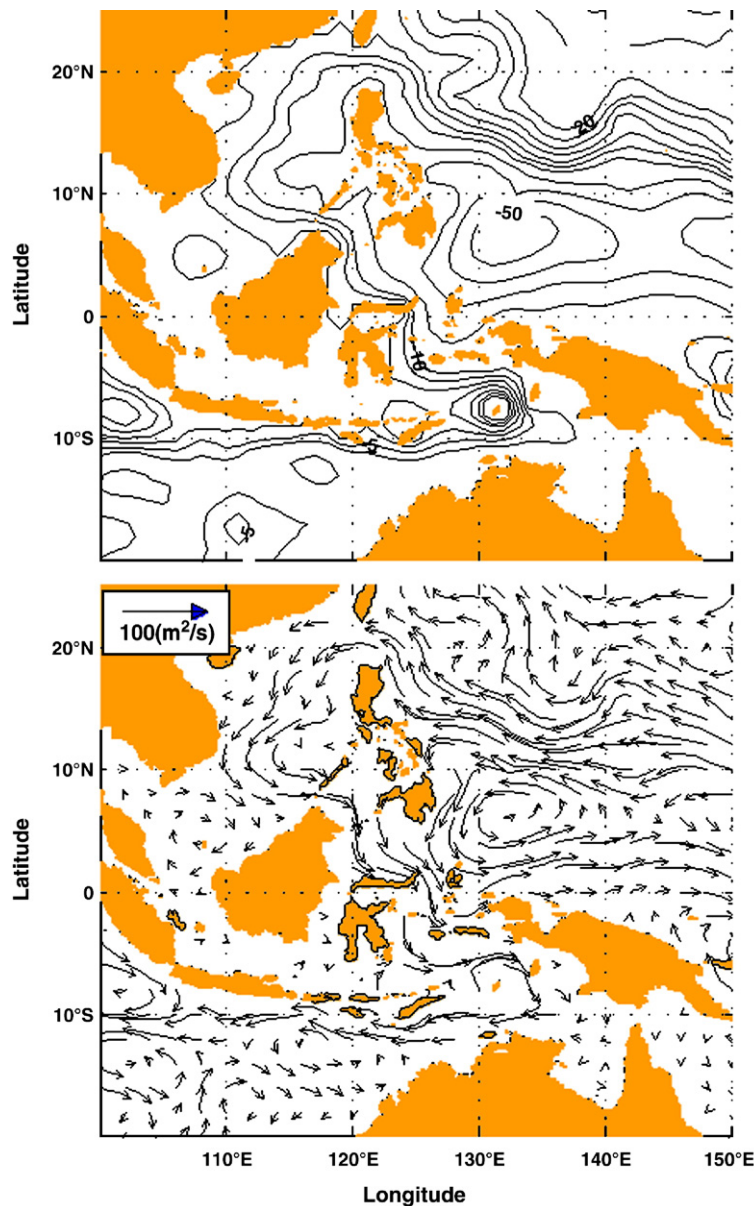

Fig. 10. Inverted annual mean Ψ and (U, V) vector fields in the vicinity of Indonesian seas.
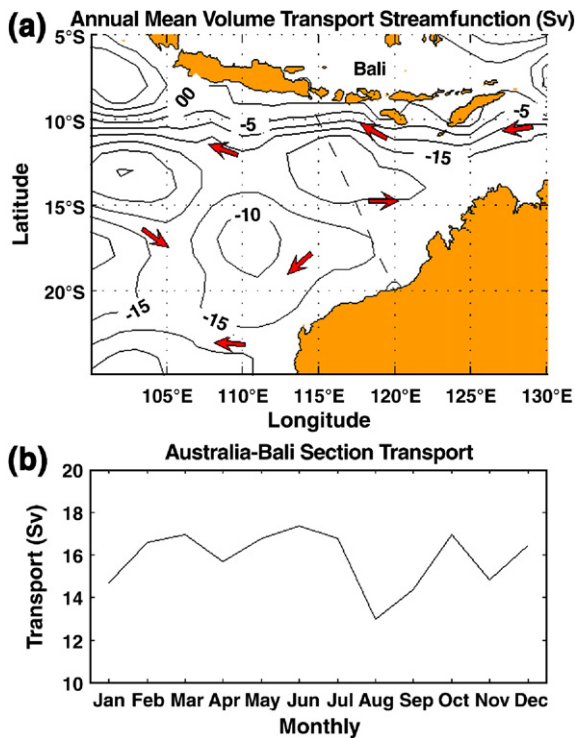
Fig. 11. Inverted volume transport between Bali (8°S, 113.5°E) and northwest coast of Australia (20°S, 120°E): (a) annual mean Ψ-field, and (b) monthly variability.

similar to surface to intermediate depth currents shown in the earlier description (e.g., Fine et al. 1994; Lukas et al., 1996; Godfrey, 1996): water from the Pacific Ocean enters the Indonesian near the region where the New Guinea Coast Current (10 Sv) meets the Mindanao Current (10–20 Sv), as well through the South Sulu Sea from the South China Sea (Fig. 10). The New Guinea Coast Current transports 10 Sv water around the Halmahera Eddy into the southeastward flowing North Equatorial Countercurrent.

The North Equatorial Current bifurcates east of the Philippines, with the southern branch becoming the Mindanao Current and the northern branch becoming the Kuroshio. Part of the water flowing southward in the Mindanao Current retroflects 10–20 Sv around the Mindanao Eddy to join the North Equatorial Counter-current, while the remainder enters the Celebes Sea, where some South Pacific water passes into the Indonesian seas near Halmahera. The majority of the Indonesian throughflow water exits to the Indian Ocean through the Timor Strait, with smaller transport through the Savu Sea and Lomok Strait. The Mindanao Eddy (cyclonic) near the southern Philippines and the Halmahera Eddy (anticyclonic) near Indonesia are

well represented in the inverted Ψ and (U, V) fields (Fig. 10). No strong flow is obtained through the Makassar Strait in the present computation that is the discrepancy with the earlier studies.

The monthly volume transport between Bali (8°S, 113.5°E) and northwest coast of Australia (20°S, 120°E) represents most of the Indonesian throughflow (Fig. 11) and shows a weak seasonal variability with a maximum value of 22.9 Sv in December and a minimum value of 20.3 Sv in August. Our estimation (Fig. 11) agrees well qualitatively with the observational data (16.2 Sv) collected along the same section (Bali to Australia) in August 1989 by Fieux et al. (1994) and with the numerical simulated data (25.7 Sv using the 1.5 reduced gravity model, 15.8 Sv using the nonlinear six-layer model) reported by Morey et al. (1999).

8.2.3. Kuroshio transport and its intrusion into the South China Sea

Difference of the Ψ-values between Japan and the center of the subtropical gyre is used as the Kuroshio volume transport (Fig. 12). The monthly Kuroshio volume transport is very steady (very weak seasonal variation) with the transport from 57.7 to 62.4 Sv (Fig. 12). Our
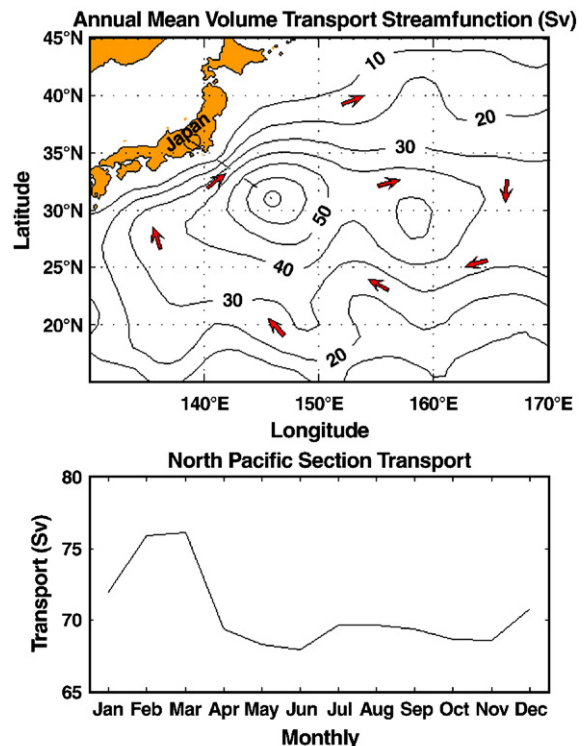

Fig. 12. Monthly variation of the Kuroshio transport.

calculation of the Kuroshio volume transport agrees with Schmitz's (1996a,b) estimation (52.4 Sv).

The seasonal variation of the intrusion of the Kuroshio Water into the South China Sea through the Luzon Strait has been investigated by many authors (e.g., Shaw, 1989; Chu and Li, 2000). Shaw (1989) used the discriminant method to classify the water mass T, S characteristics at 150, 200, and 250 m, and found that the water characteristics of the Philippine Sea (Kuroshio) were identifiable along the continental margin south of China from October to January. The presence of this water indicated an intrusion current from the Philippine Sea into the South China Sea. Chu and Li (2000) used the **P**-vector inverse method (Chu, 1995, 2000) to determine the isopycnal surface geostrophic velocities in the South China Sea. The annual and monthly mean volume transports through the Luzon Strait (Fig. 13) show Kuroshio intrusion all year round with a seasonal variation (8–15 Sv). This estimate is larger than existing estimations such as 2–3 Sv (Wyrtki, 1961), 8–10 Sv (Huang et al., 1994), 2.4–4.4 Sv (Metzger and Hurlburt, 1996), and 1.4–13.7 Sv (Chu and Li, 2000).

8.2.4. Australian Mediterranean and South Australian gyre

The (Ψ, U, V) fields (Fig. 14) shows the following features: the southward flowing East Australia Current is the western boundary current of the southern hemisphere. It is the weakest of all boundary currents, carrying only about 10 Sv. The current first follows the Australian coast, then separates from it somewhere near 34°S (the latitude of the northern end of New Zealand's North Island). This current recirculates (10 Sv) and forms an anticyclonic (anticlockwise) eddy. The path of the current from Australia to New Zealand is known as the Tasman Front, which makes the boundary of the warmer water of the Coral Sea and the colder water of the Tasman Sea. In the South Australian Basin, an anticyclonic eddy is identified and recirculates 10 Sv with a weak seasonal variation.

8.3. Atlantic Basin

8.3.1. General features

Setting aside the part of Pacific west of New Zealand and the Tonga–Kermadec Ridge, which has no counterpart in the Atlantic, there is some correspondence in the features (Figs. 4 and 5). Each basin has an anticyclonic gyre in the mid-latitudes of both hemispheres, mostly west of the major ridge, with two cyclonic gyres in between (low-latitudes).

The low-latitude dual cyclonic gyres have a larger latitudinal span in the Atlantic Basin (30°S–30°N) than in the Pacific Basin (10°S–20°N). The common branch of the dual cyclonic gyres forms the eastward flowing equatorial currents. For the Atlantic Basin, there is some correspondence between the transports north and south of the equator aside from the Caribbean and Gulf of Mexico, which has no counterpart in the South Atlantic. The mid-latitude anticyclonic gyres in the North Atlantic and the South Atlantic have a comparable strength (50 Sv). We may also identify following major features from Figs. 4 and 5: the Gulf Stream, the Labrador Basin cyclonic gyre, and the Brazil–Malvinas confluence zone.

8.3.2. Gulf Stream volume transport

The Gulf Stream volume transport can be easily identified as the difference of Ψ-values at the North Atlantic continent and at the center of the subtropical gyre. The monthly mean Gulf Stream transport is quite steady with a maximum transport of 62 Sv in October and a minimum transport of 52 Sv in March and April (Fig. 15). The calculated Gulf Stream volume transport (57 Sv) is too weak compared to the value of 120 Sv
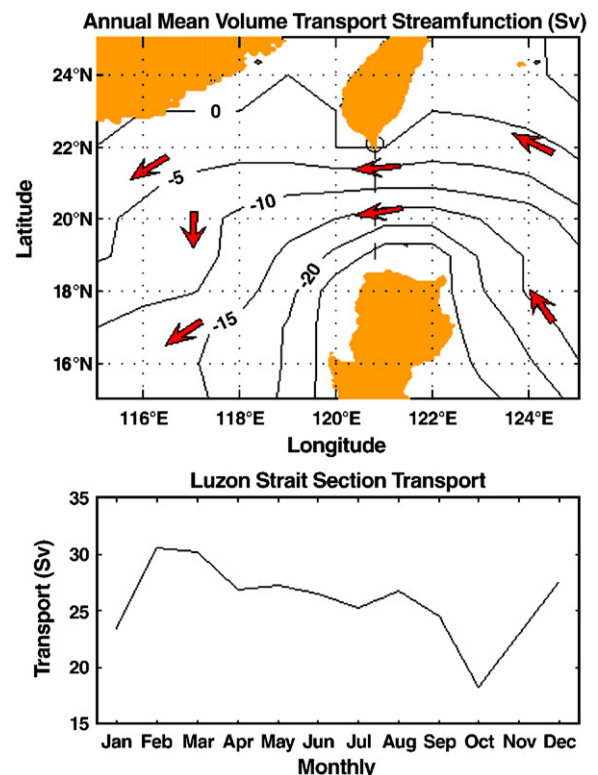

Fig. 13. Monthly variation of volume transport through the Luzon Strait into the South China Sea.

found after detachment from Cape Hatteras when encompassing the Southern Recirculation gyre transport (Hogg, 1992). This is due to the smoothed nature of the climatological wind and hydrographic data used.

8.3.3. Brazil–Malvinas confluence

From its littoral margin to the open ocean, the western South Atlantic is marked by the circulation patterns and exchange processes that are centrally important to the regional marine resources and local economics, and equally important to the global flux of heat and dissolved substances (Campos et al., 1995). The depth-integrated western boundary current (Brazil Current) originates from the South Equatorial Current (Figs. 4 and 5). A major change in the flow patterns along the western boundary occurs in the southern Brazil Basin. Among other important characteristics, the Southwest Atlantic is characterized by the presence of the Brazil Current, a warm western boundary current that, while weaker than the Gulf Stream in terms of the
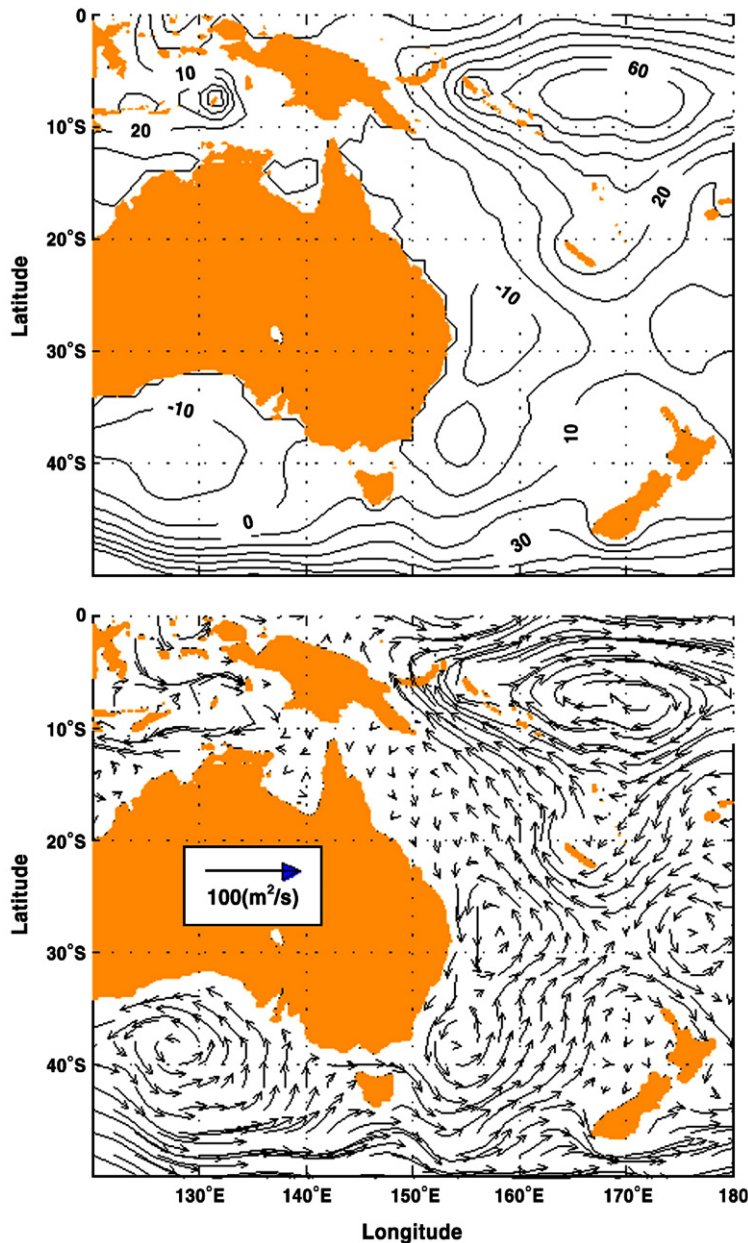

Fig. 14. Inverted annual mean Ψ and (U, V) vector fields in the vicinity of the Australian Mediterranean sea and the South Australian Basin.

mass transport, is energetically comparable to its North Atlantic counterpart, particularly in the region of confluence with the northward-flowing Malvinas Current at approximately 38°S (Fig. 16). The western limb of the recirculation cell (anticyclonic) separates from the continental slope at about 38°S upon its confluence with the northward-flowing Malvinas Current, whereupon the bulk of the Malvinas retroflects cyclonically (clockwise) back toward the southeast while lesser portions continue northeast along the coast. On the eastern side of the cyclonic trough is the combined southeastward flow of Malvinas and Brazil Current waters that extend to 45°S before the subtropical waters turn east and north to form the pole-ward limits of the subtropical gyre. The Malvinas waters continue south to the southern margin of the Argentine Basin (49°S)

before turning east with the Antarctic Circumpolar Current regime. Our results are consistent with the earlier studies (e.g., Peterson and Whitworth, 1989). The Brazil–Malvinas confluence occurs all year round with a very weak seasonal variability.

8.4. Indian Ocean

The depth-integrated circulation pattern in the Indian Ocean is depicted in Figs. 4 and 5. Here, we discuss the characteristics of the Agulhas Current System and Transport through the Mozambique Channel as examples showing the model capability. The Agulhas Current is the western boundary current in the Indian Ocean. It retroflects, meanders and sheds discrete eddies that translate into and across the South Atlantic Ocean. This
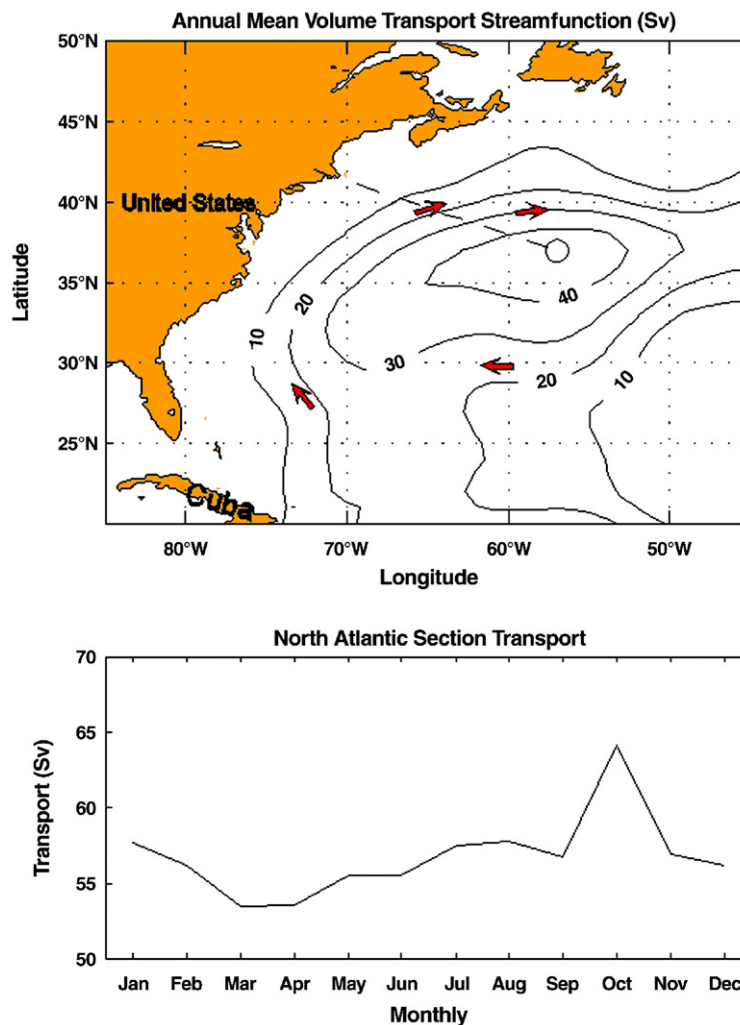

Fig. 15. Inverted monthly volume transport between the North American east coast and the center of the subtropical gyre representing the Gulf Stream transport.

is the major contributor to the inter-basin exchanges of heat and salt between the South Indian and the South Atlantic Oceans (Gordon, 1985).

8.4.1. Agulhas Current Retroflection

The model inverts the Agulhas Current System (Fig. 17) well with earlier depictions (e.g., Gordon, 1985; Schmitz, 1996a,b). The South Equatorial Current bifurcates into northward and southward branches at the

northwestern coast of Madagascar. The southward branch (East Madagascar Current) carries 20–30 Sv and merges with the western boundary current (20–30 Sv) through the Mocabique Channel to form the Agulhas Current (50 Sv). This current retroflects at 40°S near the southern tip of Africa and the return current becomes the east wing of a permanent eddy (Agulhas Eddy, anticyclonic) which recirculates 10 Sv. We also see another anticyclonic eddy (10 Sv) occurring in all
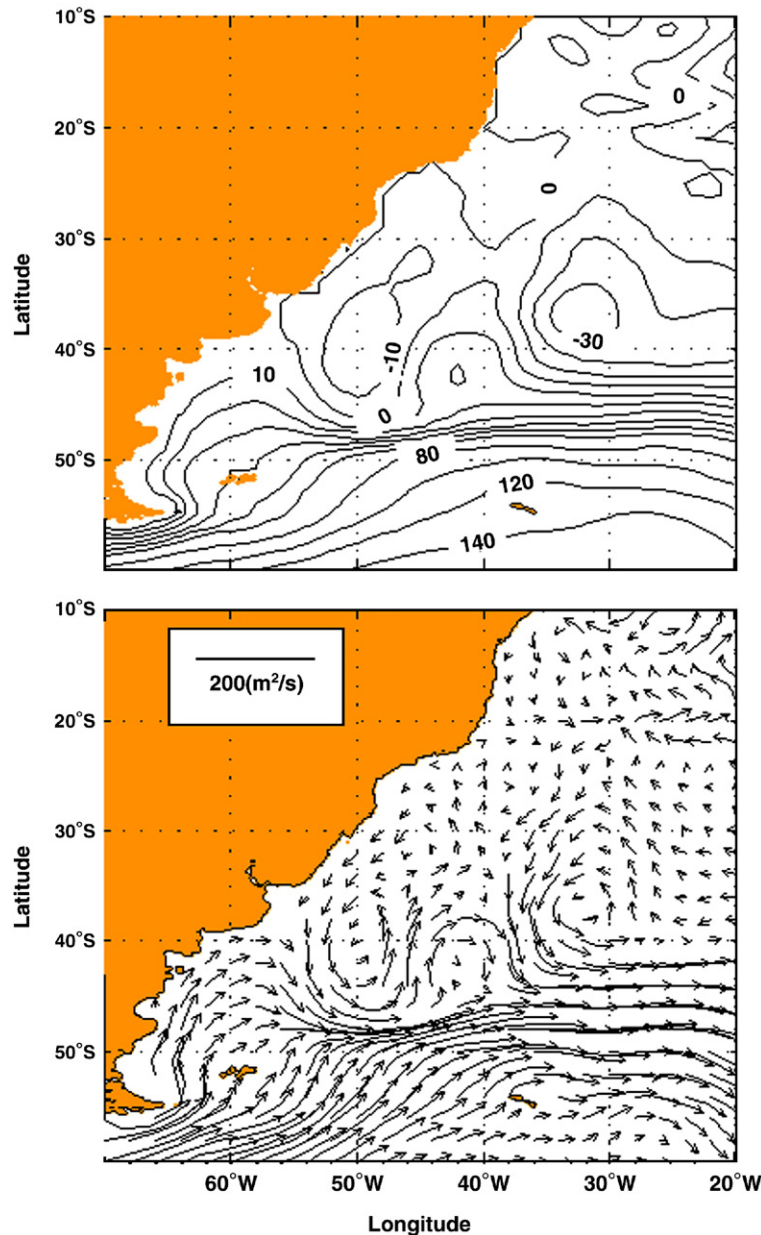

Fig. 16. Inverted annual mean Ψ and (U, V) vector fields in the southwestern South Atlantic Ocean.
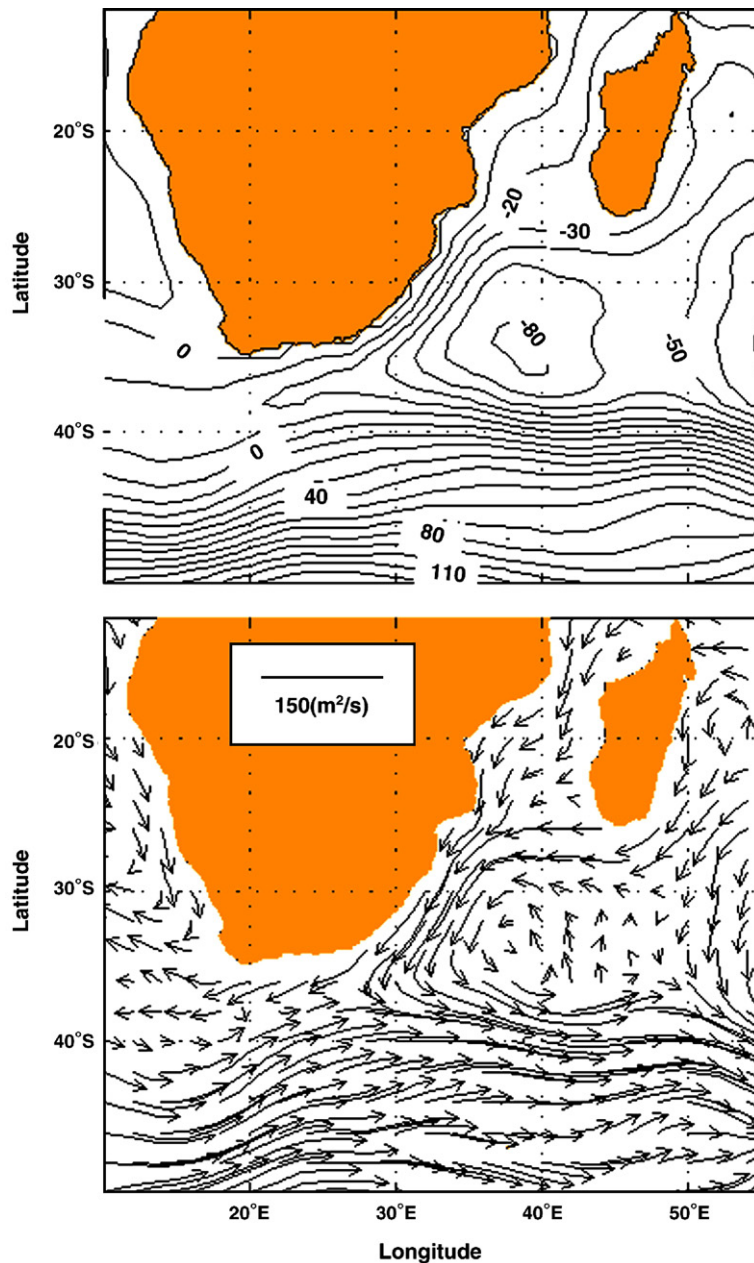
Fig. 17. Inverted annual mean Ψ and (U, V) vector fields in the vicinity of the south tip of Africa representing the Agulhas Retroflection.

monthly fields in the South Atlantic west of the south tip of Africa.

8.4.2. Transport at the Mozambique Channel

The southward flow through the Mocabique Channel is a major contributor of the Agulhas Current. The volume transport through this channel is calculated by the difference of Ψ-values for the African continent and for Madagascar. The monthly mean transport through the Mozambique Channel has a weak seasonal variation with a maximum transport of 31 Sv in December and a minimum transport of 23 Sv in August (Fig. 18).

9. Conclusions

(1) An inverse model is constructed to calculate the depth-integrated circulation and volume transport streamfunction using surface wind and
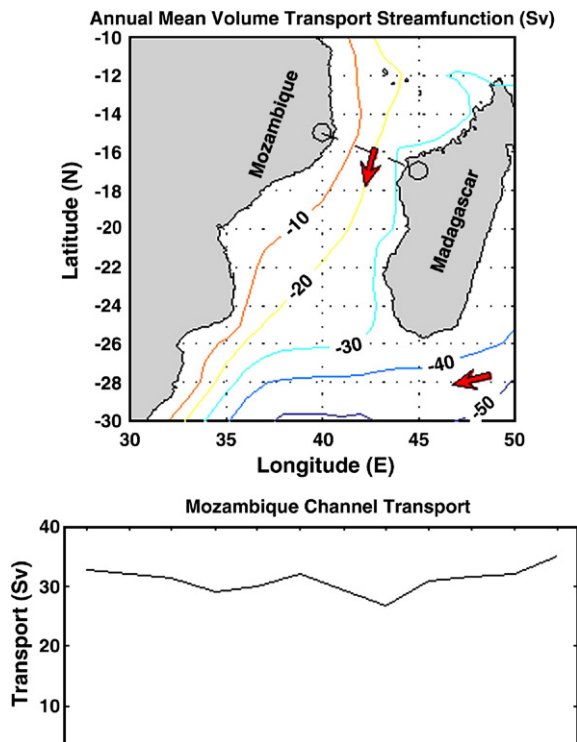
Fig. 18. Monthly mean transport through the Mozambique Channel.

hydrographic data. This model contains four major components: (a) the **P**-vector inverse model to obtain the solutions for the two extra-equatorial hemispheres (see Appendix-A), (b) the objective method to determine the Ψ-values at individual islands (see Appendix-B), (c) the Poisson equation-solver to obtain the Π-values over the equatorial region from the volume transport vorticity Eq. (30), and (d) the Poisson equation-solver to obtain the Ψ and depth-integrated velocity field (U, V) over the globe from the Poisson Ψ-equation.

(2) The Poisson equation-solver is similar to the box inverse model developed by Wunsch because both methods are based on mass conservation. The **P**-vector method provides the interim solutions with noise (appearing in the forcing terms in the Poisson equation) for extra-equatorial region and the integration of the Poisson equation (box type method) filters out the noise and provides final solutions. Thus, the proposed method has the strength from both **P**-vector and box models.

(3) This inverse model uses realistic topography and has the capability to filter out noise (in the forcing terms) since two Poisson equations are integrated. The inverted volume transport is insensitive to

noise in wind and hydrographic data. These features make it applicable for practical use.

(4) The inverted global and regional depth-integrated circulation patterns agree well with earlier studies. The monthly Ψ and (U, V) fields provide realistic open boundary conditions for regional/coastal models.

(5) An objective method is developed to determine Ψ-values at the islands on the base of Stokes circulation theorem (see Appendix-B). This method contains two components: (a) an algebraic equation for linking the Ψ-value of the island to the circulation around it and the Ψ-values in the neighboring water, (b) an iterative algorithm for determining the Ψ-value at the island. Determination of Ψ-values at islands using this objective method is not sensitive to the noise level.

Acknowledgments

Appendix A. P-vector inverse method

As pointed out by Wunsch and Grant (1982), in determining large-scale circulation from hydrographic data, we can be reasonably confident of the assumptions of geostrophic balance, mass conservation, and no major cross-isopycnal mixing (except for water masses in contact with the atmosphere). Under these conditions, the density of each fluid element would be conserved, which mathematically is given by which changes into

$$\mathbf{V} \cdot \nabla \rho = 0. \tag{A1}$$

The conservation of potential vorticity equation can be obtained by differentiating (A1) with respect to z, using geostrophic and hydrostatic balances (5) and (3), and including the latitudinal variation of the Coriolis parameter,

$$\mathbf{V} \cdot \nabla q = 0, \tag{A2}$$

where q is the potential vorticity

$$q = f \frac{\partial \rho}{\partial z}. \tag{A3}$$

It is noted that neglect of relative vorticity may induce a small but systematic error into the estimation of potential vorticity.
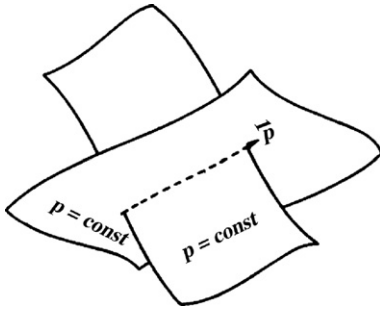
Fig. A1. Intersection of constant q and ρ surfaces and the vector **P**.

When the constant ρ surface intersects the constant q-surface (Fig. A1), it is true that

$$\nabla \rho \times \nabla q \neq 0.$$

A unit vector, called the perfect vector (or **P**-vector) by Chu (1995), can be defined by

$$\mathbf{P} = \frac{\nabla \rho \times \nabla q}{|\nabla \rho \times \nabla q|}. \tag{A4}$$

Eqs. (A1) and (A2) show that **V** is perpendicular to both $\nabla \rho$ and ∇q, and thus, **V** is parallel to **P**,

$$\mathbf{V} = \gamma \mathbf{P}, \tag{A5}$$

where γ is a scalar and its absolute value $|\gamma|$ is the speed.

A two-step method was proposed by Chu (1995) (i.e., the **P**-vector inverse method): (a) determination of the unit vector **P**, and (b) determination of the scalar γ from the thermal wind relation. Applying the thermal wind relation,

$$u = u_{-H} + \frac{g}{f \rho_0} \int_{-H}^{z} \frac{\partial \rho}{\partial y} \mathrm{d}z', \tag{A6}$$

$$v = v_{-H} + \frac{g}{f \rho_0} \int_{-H}^{z} \frac{\partial \rho}{\partial x} \mathrm{d}z'. \tag{A7}$$

at two different levels z_k and z_m (or ρ_k and ρ_m), a set of algebraic equations for determining the parameter γ are obtained

$$\gamma^{(k)} \mathbf{P}_x^{(k)} - \gamma^{(m)} \mathbf{P}_x^{(m)} = \Delta u_{km}, \tag{A8}$$

$$\gamma^{(k)} \mathbf{P}_y^{(k)} - \gamma^{(m)} \mathbf{P}_y^{(m)} = \Delta v_{km}, \tag{A9}$$

where

$$\Delta u_{km} \equiv \frac{g}{f \rho_0} \int_{z_m}^{z_k} \frac{\partial \rho}{\partial y} \mathrm{d}z', \quad \Delta v_{km} \equiv -\frac{g}{f \rho_0} \int_{z_m}^{z_k} \frac{\partial \rho}{\partial x} \mathrm{d}z'. \tag{A10}$$

If the determinant

$$\begin{vmatrix} \mathbf{P}_x^{(k)} & \mathbf{P}_x^{(m)} \\ \mathbf{P}_y^{(m)} & \mathbf{P}_y^{(m)} \end{vmatrix} \neq 0, \tag{A11}$$

the algebraic Eqs. (A8) and (A9) have unique solution for $\gamma^{(k)}(m \neq k)$,

$$\gamma^{(k)} = \frac{\begin{vmatrix} \Delta u_{km} & \mathbf{P}_x^{(m)} \\ \Delta v_{km} & \mathbf{P}_y^{(m)} \end{vmatrix}}{\begin{vmatrix} \mathbf{P}_x^{(k)} & \mathbf{P}_x^{(m)} \\ \mathbf{P}_y^{(k)} & \mathbf{P}_y^{(m)} \end{vmatrix}}. \tag{A12}$$

As soon as $\gamma^{(k)}$ is obtained, the absolute velocity **V** is easily computed using (A5).

Appendix B. Stokes circulation theorem for determining Ψ-values for islands

B.1. Stokes circulation theorem

Consider the (x, y) plane with uniform grids $(\Delta x, \Delta y)$. Let the ocean basin be represented by domains Ω and islands be represented by Ω_j ($j = 1$, ..., N) with horizontal boundaries of closed solid-wall segments of $\delta \Omega_j$, $j = 1$, ..., N. The domain Ω may have open boundaries. Fig. A2 shows a schematic illustration of such a domain with three open boundary segments, and two islands. To determine the boundary conditions for islands, McWilliams (1977) defined a simply connected fluid region between an island ($\delta \Omega_j$) and a clockwise circuit in the fluid interior ($\delta \omega_j$). Let C_j denote the closed area bounded by $\delta \Omega_j$ and $\delta \omega_j$, and $(\mathbf{n}, \mathbf{s})$ be the normal (positive outward) and tangential
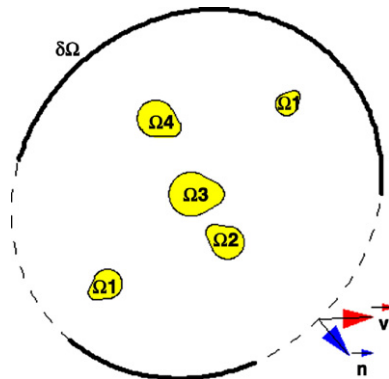

Fig. A2. A multiply connected domain. The arrows indicate the directions of integration along the line integral paths defined in the text.

unit vectors along the boundaries of C_j. The circulation around the boundary of C_j is calculated using the Stokes theorem,

$$-\oint_{\delta\Omega_j} \mathbf{V} \bullet s dl + \oint_{\delta\omega_j} \mathbf{V} \bullet s dl$$
$$= \int_{C_j} \int k \bullet (\nabla \times \mathbf{V}) dx dy, \qquad (B1)$$

where l is the path along the boundaries of C_j, $\mathbf{k}$ is the unit vector in the vertical direction, ∇ is the horizontal gradient operator. The direction of closed integration $\oint$ is defined as anticlockwise. Substitution of (27) into the first term in the lefthand side of (B1) leads to

$$\oint_{\delta\Omega_j} \nabla \Psi \bullet n dl = \oint_{\delta\omega_j} \mathbf{V} \bullet s dl$$
$$- \int_{C_j} \int k \bullet (\nabla \times \mathbf{V}) dx dy, \qquad (B2)$$

which links the Ψ-values at the island Ω_j to the surrounding velocity field. The smaller the area of C_j, the smaller the value of the second term in the righthand-side of (B2), i.e.,

$$\oint_{\delta\Omega_j} \nabla \Psi \bullet n dl \rightarrow \Gamma_j \text{ as } C_j \rightarrow 0, \qquad (B3)$$

where

$$\Gamma_j = \oint_{\delta\omega_j} \mathbf{V} \bullet s dl.$$

Thus, selection of $\delta\omega_j$ with a minimum C_j becomes a key issue in determining the streamfunction $\Psi|_{\Omega_j}$. Such

a circuit ($\delta\omega_j^*$) is called the minimum circuit along the island Ω_J (Fig. A3). Let (I_l, J_l) $(l = 1, \ldots N+1)$ be the anticlockwise rotating grid points along $\delta\omega_j^*$ with $(I_{N+1}, J_{N+1}) = (I_1, J_1)$, and let the circulation along $\delta\omega_j^*$ be denoted by $\hat{\Gamma}_j$ and computed by

$$\hat{\Gamma}_j = \frac{1}{2} \sum_{l=1}^{N} [\mathbf{V}(I_l, J_l)$$
$$+ \mathbf{V}(I_{l+1}, J_{l+1})] \bullet [i(I_{l+1} - I_l)\Delta x$$
$$+ j(J_{L+1} - J_l)\Delta y], \qquad (B4)$$

which is solely determined by the island geometry and the velocity field $\mathbf{V}$.

B.2. Algebraic equation for Ψ-value at island Ω_j

The lefthand side of (B3) is discretized by

$$\oint_{\delta\Omega_j} \nabla \Psi \bullet n dl \doteq \sum_{l=1}^{N} \frac{(I_{l+1} - I_l)\Delta x}{\Delta y} [\Psi(I_l, J_l - 1)$$
$$+ \Psi(I_{l+1}, J_{l+1} - 1) - \Psi(I_l, J_l + 1) - \Psi(I_{l+1}, J_{l+1} + 1)]$$
$$+ \sum_{l=1}^{N} \frac{(J_{l+1} - J_l)\Delta y}{\Delta x} [\Psi(I_l + 1, J_l) + \Psi(I_{l+1}$$
$$+ 1, J_{l+1}) - \Psi(I_l - 1, J_l) - \Psi(I_{l+1} - 1, J_{l+1})].$$

Since the grid points on the island Ω_j are always on the left side of the anticlockwise circulation $\hat{\Gamma}_j$ (Fig. A3),
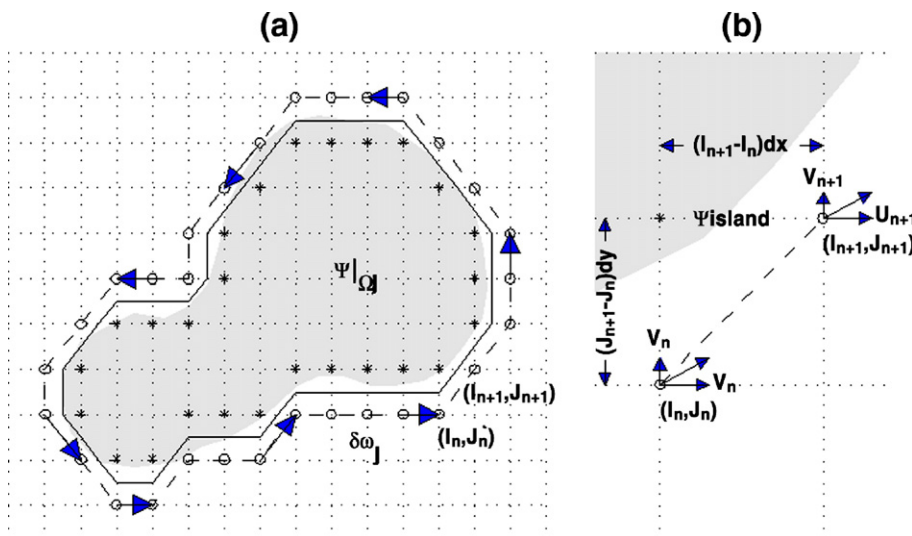

Fig. A3. Grid points of the minimum circuit along the island Ω_j.

half grid points of (A4) are in the island and half in the water. Thus, Eq. (B4) can be written by

$$\Gamma_j = A\Psi|_{\Omega_j} + \Gamma_j^{(w)}$$

where $\Gamma_j^{(w)}$ is the circulation in the water and

$$A = -\sum_{l=1}^{N} \left(\frac{|J_{l+1}-J_l|\Delta y}{2\Delta x} + \frac{|I_{l+1}-I_l|\Delta x}{2\Delta y} \right).$$

The volume transport streamfunction at island Ω_j is computed by

$$\Psi|_{\Omega_j} = \frac{\hat{\Gamma}_j - \Gamma_j^{(w)}}{A}. \tag{B5}$$

B.3. Iteration process

Eq. (B5) cannot be directly used to compute $\Psi|_{\Omega_j}$ even if the vertically integrated velocity (U, V) is given. This is because that the Ψ-values at surrounding water is still undetermined. Thus, we need an iterative process to determine $\Psi|_{\Omega_j}$ from a first guess value.

Suppose all the islands Ω_j $(j=2, ..., N)$ in Fig. A2 to be removed. With the given boundary conditions at $\delta\Omega_j$, we solve the Ψ-Poisson equation (28) and obtain the solution $\Psi^*(x, y)$. Average of Ψ^* over Ω_j leads to the first guess Ψ-values at islands Ω_j $(j=2, ..., N)$,

$$\Psi|_{\Omega_j}(0) = \int\int_{\Omega_j} \Psi^*(x, y)\mathrm{d}x\mathrm{d}y.$$

Let Ψ-values and the circulation $\hat{\Gamma}_j$ be given at the m-th iteration such that

$$\Psi|_{\Omega_j}(m) = \frac{\Gamma_j^*(m) - \sum_k B_k \Psi_k(m)}{A}, \tag{B6}$$

where the minimum circuit circulation at the m-th iteration, $\Gamma_j^*(m)$, might not be the same as $\hat{\Gamma}_j$. We update $\Psi|_{\Omega_j}$ using

$$\Psi|_{\Omega_j}(m) = \frac{\Gamma_j^*(m) - \sum_k B_k \Psi_k(m)}{A}. \tag{B7}$$

Subtraction of (B6) from (B7) leads to

$$\Psi|_{\Omega_j}(m+1) = \Psi|_{\Omega_j}(m) + \frac{\hat{\Gamma}_j - \Gamma_j^*(m)}{A}, \tag{B8}$$

which indicates the iteration process: (a) solving the Ψ-Poisson equation (28) with $\Psi|_{\Omega_j}(m)$ to obtain solutions

and in turn to get $\Gamma_j^*(m)$, (b) replacing the Ψ-values at islands using (B8). The iteration process repeats until reaching a certain criterion

$$\frac{|\delta\Gamma^*|}{|\hat{\Gamma}|} \leq \varepsilon, \tag{B9}$$

where

$$|\hat{\Gamma}| \equiv \sqrt{\frac{1}{N}\sum_{j=1}^{N} \left[\hat{\Gamma}_j\right]^2}, \quad |\delta\Gamma^*| \equiv \sqrt{\frac{1}{N}\left[\Gamma_j^*(m+1)-\Gamma_j^*(m)\right]^2}, \tag{B10}$$

and ε is a small positive number (user input), which is set to be 10^{-6} in this study. As soon as the inequality (B9) is satisfied, the iteration stops and the final set of $\{\Psi|_{\Omega_j}, j=1, 2, ..., N\}$ become the optimal Ψ-values for islands.

References

Bagriantsev, N.V., Gordon, A.L., Huber, B.A., 1989. Weddell Gyre: temperature and maximum stratum. J. Geophys. Res. 94, 8331–8334.

Baker Jr., D.J., 1982. A note on Sverdrup balance in the Southern Ocean. J. Mar. Res. 40, 21–26 (Supple).

Beckmann, A., Hartmut, H., Timmermann, R., 1999. A numerical model of the Weddell Sea: large-scale circulation and water mass distribution. J. Geophys. Res. 104, 23375–23391.

Campos, E.J.D., Miller, J.L., Muller, T.J., Peterson, R.G., 1995. Physical oceanography of the Southwest Atlantic Ocean. Oceanography 8, 87–91.

Chu, P.C., 1995. P-vector method for determining absolute velocity from hydrographic data. Mar. Technol. Soc. J. 29 (3), 3–14.

Chu, P.C., 2000. P-vector spirals and determination of absolute velocities. J. Oceanogr. 56, 591–599.

Chu, P.C., 2006. P-vector inverse method. Springer, Berlin, Germany. 605 pp.

Chu, P.C., Fan, C.W., Cai, W.J., 1998a. Evaluation of P vector method using modular ocean model (MOM). J. Oceanogr. 54, 185–198.

Chu, P.C., Fan, C.W., Lozano, C.J., Kerling, J., 1998b. An AXBT survey of the South China Sea. J. Geophys. Res. 103, 21637–21652.

Chu, P.C., Li, R.F., 2000. South China Sea isopycnal surface circulations. J. Phys. Oceanogr. 30, 2419–2438.

Chu, P.C., Lan, J., Fan, C.W., 2001a. Japan Sea circulation and thermohaline structure, Part 1 Climatology. J. Phys. Oceanogr. 31, 244–271.

Chu, P.C., Lan, J., Fan, C.W., 2001b. Japan Sea circulation and thermohaline structure, Part 2 A variational P-vector method. J. Phys. Oceanogr. 31, 2886–2902.

da Silva, A.M., Young, C.C., Levitus, S., 1994. Atlas of Surface Marine Data 1994. Tech. Rep. Geosci., vol. 94. University of Wisconsin, Milwakee. 83pp.

Deacon, G.E.R., 1979. The Weddell gyre. Deep-Sea Res. 26A, 981–995.

DeMaster, D.J., Dunbar, R.B., Gordon, L.I., Leventer, A.R., Morrison, J.M., Nelson, D.M., Nittrouer, C.A., Smith Jr., W.O., 1992. Cycling and accumulation of biogenic and organic matter in high-latitude environments: the Ross Sea. Oceanography 5, 146–153.

Fieux, M., Andrie, C., Delecluse, P., Ilahude, A.G., Kartavtseff, A., Mantisi, F., Molcard, R., Swallow, J.C., 1994. Measurements within the Pacific–Indian ocean throughflow region. Deep-Sea Res. 41, 1091–1130.

Fine, R.A., Lukas, R., Bingham, F.M., Warner, W.J., Gammon, R.H., 1994. The western equatorial Pacific - a water mass crossroads. J. Geophys. Res. 99, 25063–25080.

Foldvik, A., Kvinge, T., Torresen, T., 1985. Bottom currents near the continental shelf break in the Weddell Sea. In: Jacobs (Ed.), Oceanology of the Antarctic Continental Shelf. Antarct. Res. Ser., vol. 43. Amer. Geophys. Union, Washington, D.C., pp. 21–34.

Godfrey, J.S., 1989. A Sverdrup model of the depth-integrated flow for the world ocean allowing for island circulations. Geophys. Astrophys. Fluid Dyn. 45, 89–112.

Godfrey, J.S., 1996. The effect of the Indonesian throughflow on ocean circulation and heat exchange with the atmosphere: a review. J. Geophys. Res. 101, 12217–12237.

Godfrey, J.S., Golding, T.J., 1981. The Sverdrup relation in the Indian Ocean, and the effect on the Pacific-Indian Ocean throughflow on Indian Ocean circulation and on the East Australian Current. J. Phys. Oceanogr. 12, 771–779.

Gordon, A.L., 1985. Indian–Atlantic transfer of thermocline water at the Agulhas Retroflection. Sciences 227 (4690), 1030–1033.

Hogg, N.G., 1992. On the transport of the Gulf Stream between Cape Hatteras and the Grand Banks. Deep-Sea Res. 39, 1231–1246.

Leetmaa, A., Bunker, A.F., 1978. Updated charts of mean annual wind stress, convergences in the Ekman layers, and Sverdrup transports in the North Atlantic. J. Mar. Res. 36, 311–322.

Levitus, S., Boyer, T., 1994. World Ocean Atlas, Vol 4, Temperature. NOAA Atlas NESDIS, vol. 4. U.S. Gov. Printing Office, Washington, D.C. 117 pp.

Levitus, S., Burgett, R., Boyer, T., 1994. World Ocean Atlas, Vol 3: Salinity. NOAA Atlas NESDIS, vol. 3. U.S. Gov. Printing Office, Washington, D.C. 99 pp.

Lukas, R., Yamagata, T., McCreary, J.P., 1996. Pacific low-latitude western boundary currents and the Indonesian throughflow. J. Geophys. Res. 101, 12209–12216.

McWilliams, J.C., 1977. A note on a consistent quasigeostrophic model in a multiply connected domain. Dyn. Atmos. Ocean. 1, 427–441.

Mellor, G.L., 2003. Users guide for a three-dimensional, primitive equation, numerical ocean model. Prog. in Atmos. and Ocean. Sci. Princeton University. 53pp.

Metzger, E.J., Hurlburt, H.E., 1996. Coupled dynamics of the South China Sea, the Sulu Sea, and the Pacific Ocean. J. Geophys. Res. 101, 12331–12352.

Meyers, G., 1980. Do Sverdrup transports account for the Pacific North Equatorial Countercurrent? J. Geophys. Res. 85, 1073–1075.

Morey, S.L., Shriver, J.F., O'Brien, J.J., 1999. The effects of Halmahera on the Indonesian throughflow. J. Geophys. Res. 104, 23281–23296.

Mosby, H., 1934. The waters of the Atlantic Antarctic Ocean. Scientific Results of the Norwegian Antarctic Expeditions, 1927–1928, vol. 11. Det Norske Videnskaps-Academi I, Oslo, pp. 1–131.

Muench, R.D., Gordon, A.L., 1995. Circulation and transport of water along the western Weddell Sea margin. J. Geophys. Res. 100, 18503–18515.

Munk, W.H., 1950. On the wind-driven ocean circulation. J. Meteorol. 7, 79–93.

Nowlin, W.D., Klinck, J.M., 1986. The physics of the Antarctic Circumpolar Current. Rev. Geophys. 24, 469–491.

Peterson, R., Whitworth III, T., 1989. The subantarctic and Polar Fronts in relation to deep water masses through the southwestern Atlantic. J. Geophys. Res. 94, 10817–10838.

Pillsbury, R.D., Jacobs, S.S., 1985. Preliminary observations from long-term current meter moorings near the Ross Ice Shelf. In: Jacobs, S.S. (Ed.), Oceanography of the Antarctic Continental Shelf. Antarct. Res. Ser., vol. 43. Amer. Geophys. Unio, Washington, D.C., pp. 87–107.

Reid, J.L., 1989. On the total geostrophic circulation of the South Atlantic Ocean: flow patterns, tracers, and transports. Prog. Oceanogr. 23, 149–244.

Reid, J.L., 1994. On the total geostrophic circulation of the North Atlantic Ocean: flow patterns, tracers, and transports. Prog. Oceanogr. 33, 1–92.

Reid, J.L., 1997. On the total geostrophic circulation of the Pacific Ocean: flow patterns, tracers, and transports. Prog. Oceanogr. 39, 263–352.

Schmitz Jr., W., 1996a. On the world ocean circulation: Volume 1. Some Global Features/North Atlantic Circulation. Woods Hole Oceanogr. Inst. Tech. Report, WHOI-96-03. 141pp.

Schmitz Jr., W., 1996b. On the world ocean circulation: Volume 2. The Pacific and Indian Oceans/Global Update. Woods Hole Oceanogr. Inst. Tech. Report, WHOI-96-08. 237pp.

Semtner, A.J., Chervin, R.M., 1992. Ocean general circulation from a global eddy-resolving model. J. Geophys. Res. 97, 5493–5550.

Shaw, P.T., 1989. The intrusion of water masses into the sea southwest of Taiwan. J. Geophys. Res. 94, 18,213–18,226.

Stommel, H., 1948. The westward intensification of wind-driven ocean currents. Trans. Amer. Geophys. Union 54, 403–406.

Stommel, H., Schott, F., 1977. The beta spiral and the determination of the absolute velocity field from hydrographic station data. Deep Sea Res. 24, 325–329.

Sverdrup, H.U., 1947. Wind driven currents in a baroclinic ocean with applications to the equatorial currents of the eastern Pacific. Proc. Natl. Acad. Sci. U. S. A. 33, 318–326.

Tsuchiya, M., 1968. Upper waters of the intertropical Pacific Ocean. Johns Hopkins Oceanogr. Stud. 4, 50 pp.

Wunsch, C., 1978. The general circulation of the North Atlantic west of 50°W determined from inverse method. Rev. Geophys. 16, 583–620.

Wunsch, C., Grant, B., 1982. Towards the general circulation of the North Atlantic Ocean. Prog. Oceangr. 11, 1–59.